A Novel Population of Slow Magnetosonic Waves in the Ionosphere

Charles Lougheed Bennett[1]

[1]Lawrence Livermore National Laboratory

November 30, 2022

Abstract

Using data from the Van Allen Probe and Swarm-Bravo satellites, evidence for a persistent population of slow magnetosonic waves in the ionosphere is presented. Dispersion relations from two-fluid analyses of waves in warm plasma are used to interpret and explicate these observations. These waves appear to be continuously present and globally distributed. Their amplitudes systematically decrease with increasing altitude. The amplitudes are also correlated with longitude in a manner consistent with the global distribution of lightning strikes. Evidence for a number of narrow resonances consistent with doppler shifted Schumann resonance frequencies is presented.

A Novel Population of Slow Magnetosonic Waves in the Ionosphere

Charles L. Bennett[1]

[1]Retired from Lawrence Livermore National Laboratory.

Corresponding author: Charles L. Bennett (Charlie_Bennett@comcast.net)

Key Points:

- A globally distributed population of slow magnetosonic waves in the ionosphere has been found
- These waves are found at all local solar times with amplitudes decreasing vs altitude and correlated with longitude
- Evidence is presented that these waves are magnetic manifestations of Schumann resonances in the ionosphere

Abstract

Using data from the Van Allen Probe and Swarm-Bravo satellites, evidence for a persistent population of slow magnetosonic waves in the ionosphere is presented. Dispersion relations from two-fluid analyses of waves in warm plasma are used to interpret and explicate these observations. These waves appear to be continuously present and globally distributed. Their amplitudes systematically decrease with increasing altitude. The amplitudes are also correlated with longitude in a manner consistent with the global distribution of lightning strikes. Evidence for a number of narrow resonances consistent with doppler shifted Schumann resonance frequencies is presented.

Plain Language Summary

Using satellite data, just as the acoustic noise from distant lightning is heard to rumble, sometimes a considerable time later, for a much longer duration than the visible flashes, an even more greatly delayed and spread-out series of plasma-sound waves are found in the earth's ionosphere after every lightning bolt. The noise of these plasma-sound waves is found to be always present over the entire globe. Properly accounting for this noise in satellite electromagnetic field measurements could improve the quality of measurements of the earth's magnetic field from space, and lead to a better understanding of our earth's magnetic field and its ionosphere.

1 Introduction

The mean global rate of lightning is 60 flashes/s (Burgesser, 2017) and is concentrated most strongly in the mid-latitude continental regions. The high global rate of lightning strokes, together with the low attenuation at low frequencies leads to the establishment of standing wave resonances within the Earth Ionospheric Waveguide (EIWG). Within the EIWG, the wave attenuation in the frequency range below 100 Hz is roughly 0.5 dB/Mm according to (Chapman et al.,1966), so that such low frequency waves may travel several times around the globe before losing most of their energy. The propagation of electromagnetic waves in the EIWG is discussed in (Jackson, 1975), (Budden, 1957) and (Schumann, 1952). The resonances of the EIWG are known as the Schumann resonances (SRs). The transient vertical electric and horizontal magnetic fields at great distances from an individual strong lightning strike appear as exponentially damped sinusoids, designated Q-bursts by (Ogawa et al., 1967).

If the EIWG was a lossless, perfectly spherical cavity, the SR eigenfrequencies would be

$$f_n = \frac{c}{2\pi R_e}\sqrt{n(n+1)}\,, \tag{1}$$

where R_e is the Earth's radius, c is the speed of light and n is the number of the eigenmode. In the actual EIWG, the frequencies of the lowest eigenmodes are only slightly lower than the values given by equation 1, with observed values for the five lowest eigenmodes of 7.8, 14.1, 20.3, 26.3 and 32.5 Hz as listed in table 1 of (Chapman, 1966). The corresponding quality factor Q values are 4, 4.5, 5, 5.5 and 6 for these resonances. The SR intensities observed at a fixed location have significant diurnal and seasonal variations in amplitude, sometimes over a factor of two (Fullekrug M. , 1995) as the global rate of lightning varies as the subsolar point crosses the three main continental regions (Satori, 1996), (Rodriguez-Camacho et al., 2021). From the quality of the correlation between the observed intensity of the SRs and the instantaneous lightning rate (Boldi et al., 2017) no evidence is found for contributions other than lightning to the intensity of the SRs in the EIWG. Measurements of the magnetic field intensity of the lowest SR at ground level are typically less than 1 pT/Hz$^{1/2}$, e.g. (Boldi et al., 2017), (Price, 2016), (Salinas et al., 2016), (Fullekrug & Fraser-Smith, 1996), (Fullekrug, 1995), (Rodriguez-Camacho et al., 2021), and (Sentman, 1987).

Some portion of the low frequency electromagnetic energy of the SRs may penetrate through the EIWG upper boundary (EIWGUB) in the form of plasma waves. Evidence for this was sought and first claimed by (Ni & Zhao, 2005) based on measurements of electric and magnetic field data from the Aureol-3 satellite. The Aureol-3 satellite polar orbit covered an altitude range from 400km to 2,000km with an inclination of 82.5°. The claims of Ni and Zhao were not believed by (Surkov et al., 2013) for a couple of reasons. First, the spectral amplitudes at 8 Hz were *thought* to be too high: B ~ 45 pT/Hz$^{1/2}$ and E ~ 20 μV/m/Hz$^{1/2}$. Second, the peak frequencies seen in the magnetic fields did not match SR frequencies measured at ground level. However, Surkov et al. did not consider either the profound impact of doppler shifts on the SR frequencies or the possibility of passage through plasma bubbles. It will be shown below that these factors could possibly have played a role in the Ni and Zhao observations.

Later analysis by (Simoes et al., 2011) of electric field data from the C/NOFS satellite provided a more compelling case for the presence of SR electric field signatures in the ionosphere. The C/NOFS satellite had a 401 km perigee, 852 km apogee and 13° inclination. These signatures were observed throughout the ~3-year lifetime of the C/NOFS satellite with a typical electric field spectral density of 0.3 (μV/m)/Hz$^{1/2}$, which is nearly three orders of magnitude weaker than the observations near the earth's surface of the SR standing wave amplitudes.

The three Swarm satellites, *Alpha*, *Bravo* and *Charlie*, (SwA, SwB and SwC) launched in November 2013 by the European Space Agency had the mission objective to provide the best ever survey of the geomagnetic field and its temporal evolution, (Friss-Christensen et al., 2006). In a comparison (Finlay et al., 2020) of the quality of the agreement between a sophisticated model of the time-dependent near-earth geomagnetic field and the Swarm, CryoSat-2, CHAMP, SAC-C and Oersted satellites, the Swarm data indeed had the smallest rms differences between model and observations. The mean Swarm rms value for along-track field differences over all three satellites and all three field components was only 0.26 nT, while CHAMP's mean was 0.39 nT. The high quality of the Swarm magnetic field measurements was achieved despite early challenges with unexpected Sun-driven disturbances (Toffner-Clausen et al., 2016).

At 21:01:30 on 14 March, 2014 two days after SwB was raised to its operational altitude of 525 km, a mysterious chirping in the high rate SwB VFM-y channel data suddenly appeared. Exactly at the time that this chirping appeared, the overall noise level also suddenly increased slightly. This overall noise level was not significantly different between the dayside and nightside of the orbits and did not depend on longitude. The mysterious chirping just as suddenly ceased at 11:17:53 on 25 June, 2014. The cessation of chirping coincided with a manual power cycling of the VFM instrument on SwB. According to (European Space Research and Technology Centre, 2018), at the time that the chirping disappeared from the data, it is stated "70pT noise in y-measurement since [14 March 2014]". After this power cycling, the overall background noise level in the y channel returned to that seen before the onset of chirping. The overall background noise levels in the x and z channels did not significantly change after the power cycle. It will be suggested below that this mysterious chirping might be associated with SRs.

Although primarily designed to study the magnetosphere (Mauk et al., 2013) rather than the ionosphere, the perigee of the Van Allen Probes A and B (VAP-A and VAP-B) of approximately 575 km is close to the SwB altitude. In the last months of the VAP mission in 2019, the perigees of VAP-A and VAP-B were lowered to approximately 275 km and lower ionospheric data was acquired. Because of the higher sensitivity and higher sampling rate of the VAP-A & B EMFISIS (Kletzing et al., 2013) detectors, near perigee this data can be used to investigate and corroborate the nature of the mysterious SwB chirping.

In this article, evidence is presented that the mysterious SwB chirping could be associated with a globally distributed population of slow magnetosonic waves present throughout the ionosphere that is also seen in VAP data. To this author's knowledge, this population has not been previously recognized in the literature. It is suggested that these are associated with Schumann resonant standing waves that have been partially converted to slow magnetosonic waves upon passage into the ionosphere. In **section 2** of the present work, a discussion of various theoretical models is given to better understand and interpret the satellite observations. First, the two-fluid model of De Jonghe & Keppens (2020a) is reviewed as it provides an illuminating picture of the nature of the plasma waves that may propagate in the ionosphere. Then the importance of doppler shift effects for plasma waves having speeds comparable to or much less than satellite speeds is discussed. Concluding the theoretical section, an overview of the propagation of Lightning Generated (LG) waves from strike to satellite is presented. In **section 3** analysis of data from the VAP satellite mission leads to the conclusion that slow magnetosonic noise is present in the ionosphere throughout the seven-year lifetime of the VAP mission. In **section 4** analysis of the Swarm data is provided. It is suggested that the mysterious chirping is consistent in frequency with Schumann resonances that have been doppler shifted by the relative velocity between satellite and waves.

2 Theoretical Analysis

2.1 Two Fluid Plasma Model

In De Jonghe and Keppens (2020a), using a fully relativistic treatment for a two-fluid warm ion-electron plasma, a polynomial dispersion relation of sixth degree in the squared frequency ω^2 and fourth degree in squared wavenumber k^2 results. This dispersion relation is a function of five parameters: the electron and ion cyclotron frequencies, the electron and ion sound speeds and the propagation angle between the wavevector $\mathbf{k}$ and the ambient magnetic field $\mathbf{B_0}$ vector. These authors provide comprehensive expressions for the polynomial coefficients in terms of these five parameters, so that explicit solutions to the dispersion relation are found for a given wavenumber as roots of the sixth order polynomial in ω^2. It is shown in De Jonghe & Keppens (2020a) that for oblique propagation angles, the frequency ordering of the six modes corresponding to the six roots of the sixth order polynomial are fixed in the order

$$\omega_S \leq \omega_A \leq \omega_F \leq \omega_M \leq \omega_O \leq \omega_X. \tag{2}$$

The S, F and A labels refer to the Magnetohydrodynamic (MHD) slow magnetosonic (MS), fast MS and Alfven waves, while M stands for the modified electrostatic waves, O represents "ordinary" and X represents "extraordinary" electromagnetic modes. In the following discussion of the lower frequency waves propagating in the earth's ionosphere, only the MHD wave types are of present interest. In the figures and text these three MHD wave modes are green for ***S*** slow MS, red for ***A*** Alfven and blue for ***F*** fast MS waves. Representative dispersion relations using De Jonghe and Keppens (2020a) model for a typical ionospheric composition are shown in figure 1. The specific values shown were computed using the (COSPAR, 2022) model estimates for the case of the data acquisition shown in **figure 5** below. For these conditions, the wave normal surfaces are shown in figure 2 for frequencies below, near and above the transition between the short and long wavelength limits.

In figure 1 four regions of dispersionless behavior are seen in **1c**, **1f** and **1i**: for a limited range of frequencies above Ω_x ***A*** waves are nearly dispersionless, and below Ω_x all three modes ***F***, ***A*** and ***S*** become dispersionless in the long wavelength limit. Five regions of dispersive or "whistling" behavior are seen: descending frequency ***F*** whistling above Ω_x, ascending frequency ***A*** whistling below and asymptotic to Ω_x from below, ascending frequency ***A*** whistling starting a few orders of magnitude above Ω_x, descending frequency ***A*** whistling above and asymptotic to Ω_x from above, and finally ascending frequency ***S*** whistling below and asymptotic to $\Omega_x\cos(\theta)$ from below. For typical ionospheric conditions, although the ***F*** wave dispersion constant depends on plasma density and magnetic field strength, it is relatively insensitive to ion species or temperature.

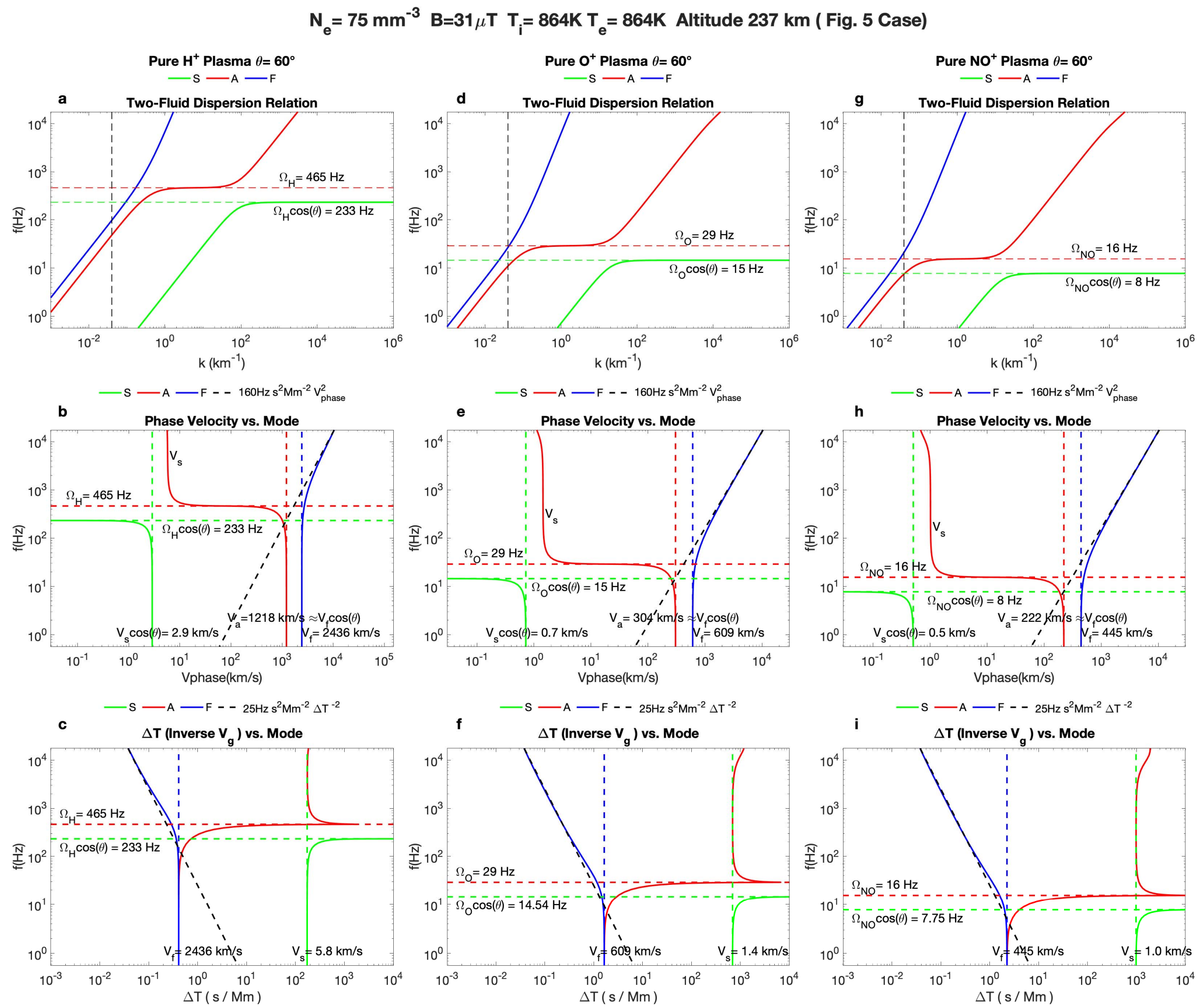

Figure 1. Dispersion relations computed from the De Jonghe and Keppens (2021a) two-fluid model are shown. The plasma parameters in the figure title are typical ionospheric conditions that correspond approximately to the conditions for the data shown in **figure 5**. The angle between the magnetic field and wavevector direction is θ. The three MHD wave modes are shown in green for ***S*** slow MS, red for ***A*** Alfven and blue for ***F*** fast MS waves. In **a**, **d** and **g**, the wave frequency is shown as a function of the wavenumber for the ion species listed in the legends. The cyclotron frequencies for each ion species are indicated next to the Ω_x labels. In **b**, **e** and **h** the frequency vs. phase velocity V_p is plotted with low frequency limit values for the slow, Alfven and fast velocities (V_s, V_a and V_f) indicated on each plot. In **c**, **f** and **i**, the frequency vs. inverse group velocity V_g is plotted. The dashed lines in **b**, **e**, **h** and **c**, **f**, **g** show that the dispersion constants indicated in the legends reasonably fit the whistling regions for all three ion species.

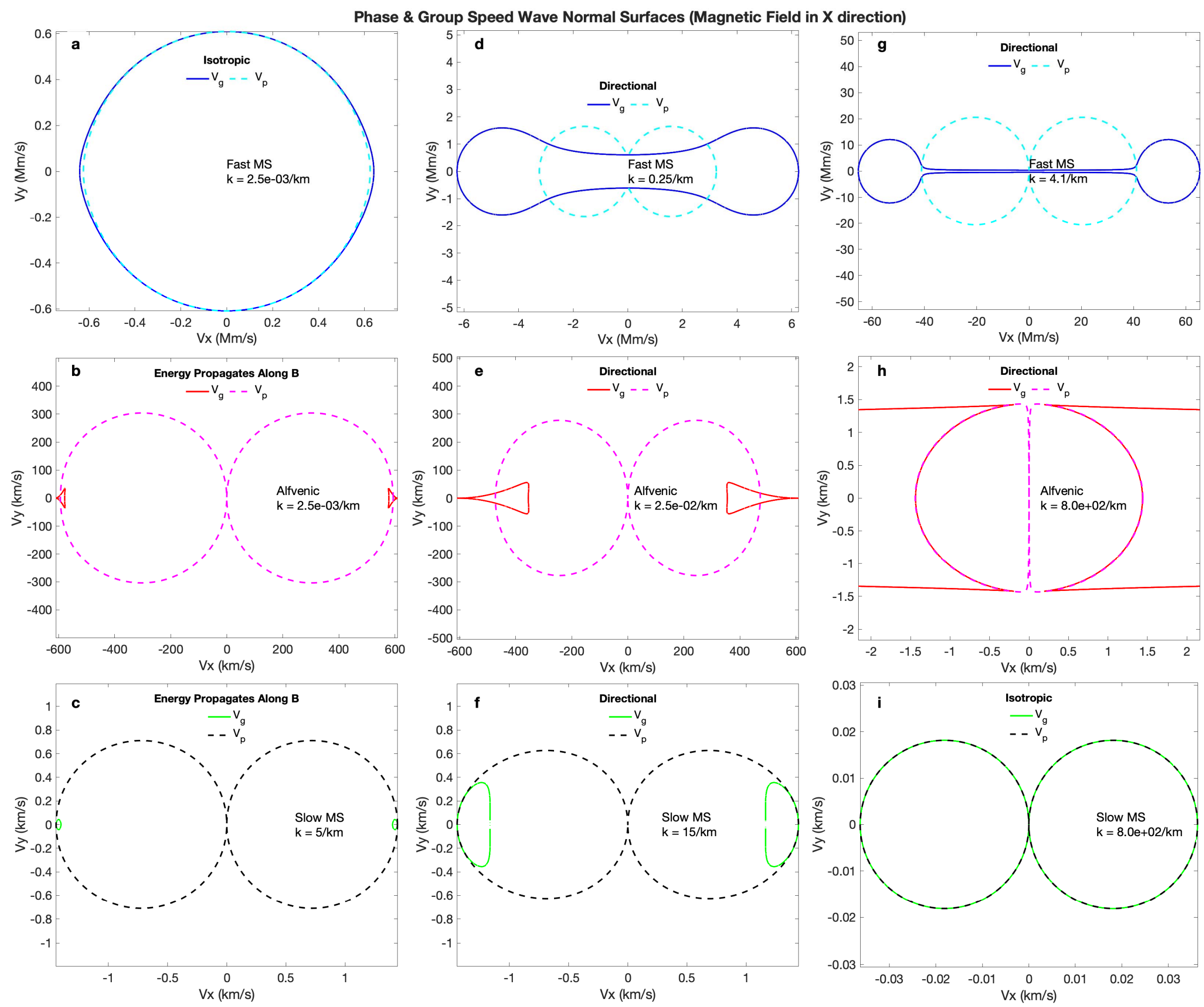

Figure 2. The wave normal surfaces for phase and group velocity in a pure O^+ plasma are shown using the same plasma parameters as previous figure. The coordinate plane is chosen to contain the phase and group velocity vectors as well as the magnetic field vector with the x axis along the ambient magnetic field direction. In **a**, **d** and **g** are shown the wave normal surfaces for the ***F*** waves for three choices of wavenumber. In **b**, **e** and **h** the wave normal surfaces for ***A*** waves are shown while in **c**, **f** and **i** the ***S*** wave normal surfaces are shown. In each of the subplots a characterization of the general behavior is given in the legend title.

The specific angle choice in figure 1 and the specific wavenumber choices in figure 2 are chosen to illustrate the transitions in the nature of the wave propagation from long wavelength to short wavelength behavior for each of the wave types. It can be seen from **2a**, **2d** and **2g** for ***F*** waves that they undergo a transition from isotropic to anisotropic behavior as the wavenumber crosses the ion cyclotron resonance. In contrast, for both ***A*** and ***S*** waves in the low wavelength limit, c.f. (Goedbloed et al., 2019) figure 5.3, energy only flows directly along magnetic field lines as the relation

$$V_p = V_g \cdot \cos(\theta) \quad (3)$$

between phase and group velocity holds. For ***A*** waves this relation is independent of temperature, while for ***S*** waves, this relation holds for ion thermal speeds much less than the speed of light.

2.2 Doppler Shifts

In general, the observed frequency of a plasma wave seen by an observer moving at velocity $\boldsymbol{V}_o$ ***relative to the plasma*** is

$$\omega_o = \omega - \boldsymbol{k} \cdot \boldsymbol{V}_o = \omega - k\, V_o\, \hat{\boldsymbol{k}} \cdot \hat{\boldsymbol{V}}_o \ . \quad (4)$$

The observed frequency relative to the emitted frequency can be written in terms of the magnitude of the phase velocity $V_p = \omega / k$ as

$$\frac{\omega_o}{\omega} = 1 - \frac{V_o\ \hat{\boldsymbol{k}} \cdot \hat{\boldsymbol{V}}_o}{V_p} \, . \quad (5)$$

For ***A*** and ***S*** wave types following equation 3, the observed to emitted doppler frequency ratio *DFR* is

$$DFR = \frac{\omega_o}{\omega} = 1 - \frac{V_o\ \hat{\boldsymbol{k}} \cdot \hat{\boldsymbol{V}}_o}{V_g\ \hat{\boldsymbol{k}} \cdot \hat{\boldsymbol{B}}_{\boldsymbol{0}}} \, . \quad (6)$$

For $\hat{\boldsymbol{k}}$ uniformly but randomly distributed over all directions, and for an angle $\boldsymbol{\gamma}$ between $\hat{\boldsymbol{V}}_o$ and $\hat{\boldsymbol{B}}_{\boldsymbol{0}}$, the probability distribution function pdf of *DFR* derived from expression 6 (details of this derivation are in the supporting information) is a Lorentzian function

$$pdf \propto \frac{1}{\left(DFR - 1 + \frac{V_o}{V_g}\cos(\gamma)\right)^2 + \left(\frac{V_o}{V_g}\sin(\gamma)\right)^2} \, . \quad (7)$$

Satellite speeds and possible plasma drift speeds in the ionosphere are so much less than *fast* plasma waves that their *DFR* values are only narrowly distributed about unity. In stark contrast, *slow* ionospheric plasma wave speeds may be comparable to (for H^+ plasmas) or substantially less than (for O^+ or NO^+ plasmas) ionospheric satellite speeds. For slow waves the distribution of *DFR* values is thus strongly dependent on the orbital inclination angle. For satellites in low inclination orbits, such as the Van Allen Probes, $\boldsymbol{\gamma}$ is nearly ±90°, so that *DFR* values are peaked near unity, but have distribution HWHM (half width at half max) = V_o/V_g values that may become very broad, such as for waves in a predominantly O^+ plasma. For satellites in nearly polar orbits, such as the Swarm satellites, γ is near 0° at the ascending node and near 180° at the descending node. In either case the widths, being proportional to sin(γ), are much narrower. As a result, for the Swarm satellites, near the ascending nodes, for slow H^+ plasma waves for which V_o/V_g is near unity, *DFR* values near 0 dominate, while near the descending nodes, *DFR* values near 2 are dominant. This rather surprising difference between ascending and descending nodes seems to appear in some Swarm satellite data, as discussed in **section 4**.

Finally, at the magnetic poles, occasionally crossed by satellites having high inclination orbits, the satellite velocity becomes perpendicular to the magnetic field direction, so that the mean *DFR* value become unity and the underlying frequencies of possible resonance may be seen, albeit with increased widths. The derivation of the Lorentzian distribution, based on the assumption of wavevectors uniformly distributed over all directions may no longer be valid in the polar region however, since lighting strikes are primarily concentrated in a band some tens of degrees wide about the equator. Thus, most lightning generated waves reaching the polar regions would have meridionally aligned wavevectors.

2.3 Random Phase Approximation for Phase Velocity

For the analysis of superpositions of large numbers of waves having uncorrelated phases the random phase approximation (RPA) has been found (Shapiro et al., 2004) particularly useful. In RPA, off diagonal elements of spectral correlations are neglected. For the electric and magnetic components having frequency f, angular frequency $\omega = 2\pi f$, Faraday's law leads to

$$\boldsymbol{k} \times \boldsymbol{E}(\mathrm{f}) = \omega \boldsymbol{B}(\mathrm{f}). \tag{8}$$

Thus, the dot product of equation (8) with the conjugate magnetic field amplitude divided by the magnitude *k* of the wave vector in RPA leads to the expression

$$V_p = \omega/k = \widehat{\boldsymbol{k}} \times \boldsymbol{E}(\mathrm{f}) \cdot \boldsymbol{B}^*(\mathrm{f})/[\boldsymbol{B}(\mathrm{f}) \cdot \boldsymbol{B}^*(\mathrm{f})], \tag{9}$$

which can be written in terms of the angles α between $\widehat{\boldsymbol{k}}$ and $\widehat{\boldsymbol{E}}$ and β between $\widehat{\boldsymbol{k}} \times \widehat{\boldsymbol{E}}$ and $\widehat{\boldsymbol{B}}$ as

$$V_p = \sin(\alpha)\cos(\beta)\,|\boldsymbol{E}(\mathrm{f})|/|\boldsymbol{B}(\mathrm{f})| \leq |\boldsymbol{E}(\mathrm{f})|/|\boldsymbol{B}(\mathrm{f})|\ , \tag{10}$$

for the magnitude of the phase velocity. The ratio of electric to magnetic magnitudes thus provides an upper limit to V_{phase}. From this expression, together with the observation that slow plasma wave speeds V_s are typically orders of magnitude less than V_f speeds in the ionosphere, slow waves are more readily detected in the magnetic field amplitudes than in the electric field amplitudes and vice versa for fast waves.

2.4 Lightning Generated Energy Propagation into the Ionosphere

The energy produced by a lightning stroke passes through a wide variety of conditions as it propagates away from the source region and enters the ionosphere as illustrated in **figure 3**. Energy radiates away from the source in a complex pattern. Electromagnetic energy in the near field region propagates approximately isotropically (above the earth's surface) for distances less than the height of the ionosphere. At greater distances, the EIWG bounded by solid earth below and the EIWGUB above, substantially affects electromagnetic wave propagation. According to (Nickolaenko et al., 2008), the expanding circular wavefront within the EIWG starts to converge after passing the "equatorial distance" of 10 Mm, reaches a local minimum amplitude at 15.5 Mm, then subsequently increases in amplitude from geometrical focusing, finally reaching a local maximum in intensity at the antipodal location. The group velocity for these waves is found (Nickolaenko & Rabinowicz, 2004) to be 0.266 Mm/s in both the expanding and converging regions. Where conditions are conducive to penetration through the EIWGUB, ***F*** mode plasma waves, able to propagate in arbitrary directions to the local magnetic field, refract at the EIWGUB and travel along nearly vertical paths (Santolik et al., 2009), (Jacobson et al., 2011) as indicated by the dashed blue line in **figure 3**. In contrast, low frequency ***S*** and ***A*** waves, constrained to follow magnetic field lines, travel different paths as indicated by the dashed red line.

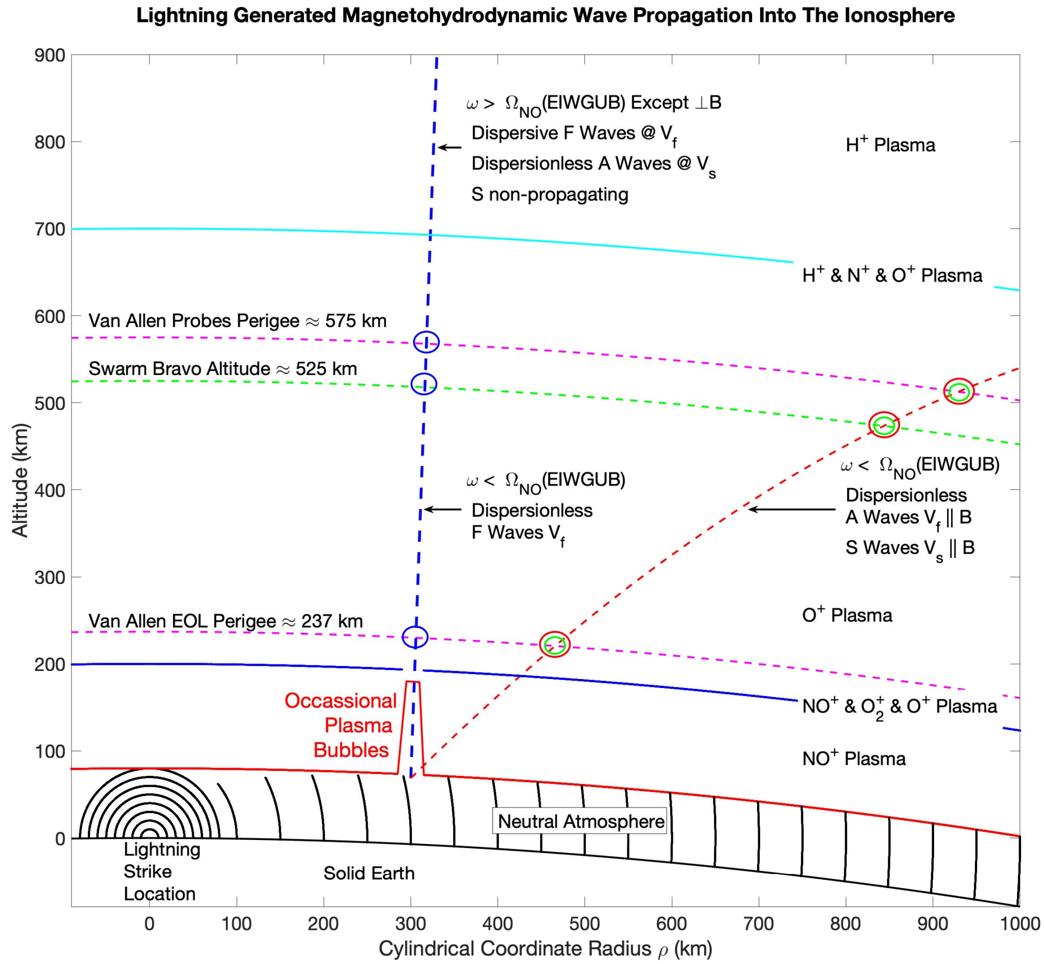

Figure 3. A schematic illustration of the propagation of LG waves through the atmosphere is shown. The "Neutral Atmosphere" indicated region forms the EIWG, in which most of the power of LG electromagnetic waves propagate. At the EIWGUB, energy in the form of plasma ***F*** waves may refract nearly vertically, as dictated by the much slower propagation velocity at the entrance to the ionosphere than in the EIWG. Plasma ***S*** waves and low frequency ***A*** waves constrained by the magnetic field follow a curved path through the ionosphere. The low/high frequency boundary happens to be roughly the cyclotron frequency for the dominant NO^+ ion species at the EIWGUB. With increasing altitude above the EIWGUB, the ionospheric composition changes substantially as indicated here by the various mixtures of ions called out in this figure. As the plasma parameters change with altitude, the wave propagation speeds V_s and V_f change but the qualitative separation between nearly vertical ***F*** waves and field aligned ***S*** and ***A*** waves persists. The Swarm-Bravo (SwB) altitude and the perigee of the Van Allen probes, both during the main mission and near the end of life (EOL), are indicated by the green and magenta curved dashed lines respectively.

In **figure 4**, the plasma conditions computed using the (COSPAR, 2022) model of the International Reference Ionosphere (IRI) are shown as a function of altitude for a representative time and location corresponding to the data shown in **figures 5**, **6** and **7** at the altitude highlighted with asterisks in **figure 4**. Also shown in this figure are the two-fluid estimates for the fast and slow MS speeds V_f and V_s as a function of ion species. Because there are generally one or more local minima in V_f as a function of altitude, “trapping regions” (Chen & Thorne, 2012) such as indicated by the horizontal dashed line in **4d**, may form, within which plasma waves may reflect one or more times between upper and lower altitude limits. Such reflections can produce “echoes” (Chum et al., 2009) such as those appearing in **figure 5**.

312

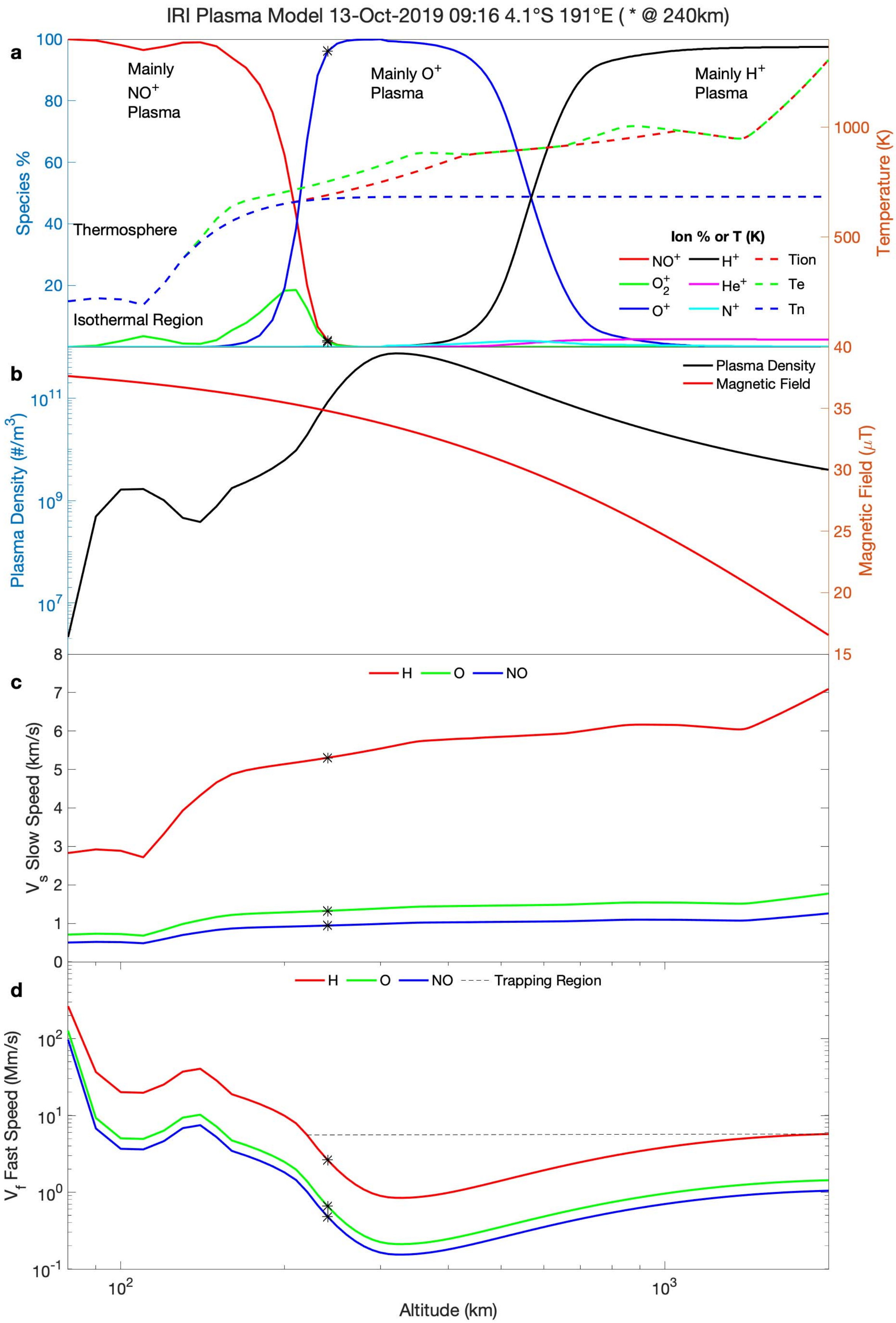
IRI Plasma Model 13-Oct-2019 09:16 4.1°S 191°E (* @ 240km)
a
Mainly NO+ Plasma
Mainly O+ Plasma
Mainly H+ Plasma
Thermosphere
Isothermal Region
Species %
Temperature (K)
Ion % or T (K)
NO+
O2+
O+
H+
He+
N+
Tion
Te
Tn
b
Plasma Density
Magnetic Field
Plasma Density (#/m3)
Magnetic Field (μT)
c
H
O
NO
Vs Slow Speed (km/s)
d
H
O
NO
Trapping Region
Vf Fast Speed (Mm/s)
Altitude (km)

Figure 4. The plasma conditions are shown as a function of altitude for the time and location specified in the figure title. In **a** the ion species, ion, electron, and neutral temperatures are shown. In **b** the magnetic field strength and plasma density are shown. In **c** the two-fluid estimates for V_s are shown for the three dominant ion species. In **d** the two-fluid estimates for V_f are shown.

In all cases in this work, the Alfven speed is nearly identical to V_f. At certain times and locations, "bubbles" of much lower plasma density may be found (Woodman, 2009), in which the electron density may drop several orders of magnitude below surrounding plasma values and in which V_f may rise by orders of magnitude. Slow wave speeds V_s, in contrast to V_f, are relatively unaffected by such plasma bubbles. Such bubbles may sometimes extend to the base of the ionosphere, as schematically illustrated in **figure 3**.

3 Plasma Wave Observations Using Van Allen Probe Data

3.1 Van Allen Probe Observations in the Ionosphere

The pair of Van Allen Probes A and B (VAP-A and VAP-B) were launched on 30 Aug 2012 into highly elliptical orbits with apogee approximately 30.6 Mm, inclination approximately 18° and perigee altitudes of approximately 575 km. In the last months of the VAP mission in 2019, the perigees were lowered to approximately 275 km. Because of the high sensitivity and high sampling rate by the Van Allen probe (Mauk et al., 2013) EMFISIS (Kletzing et al., 2013) detectors, their data is most useful for plasma wave observations. One of the EMFISIS data products comprises a series of "onboard survey mode" acquisitions at 6 second intervals derived from the first 0.4681 seconds of each survey interval. These acquisitions provide the full set of magnetic (Bu, Bv, Bw) and electric (Eu, Ev, Ew) field cross spectral matrix elements, with 6 diagonal power spectral densities (PSDs) and 15 off-diagonal elements over a logarithmically distributed range of frequencies. Another EMFISIS data product comprises a series of "burst mode" acquisitions, with 35 kHz sampling of all three components of the electric and magnetic fields over a period of 6 seconds. Each such burst comprises a set of 208,896 samples at a rate of 35kHz. Contiguous bursts have a dead time gap of 0.0315s between bursts. During the VAP mission, long (~10 minute) intervals of contiguous bursts were usually not acquired. Occasionally, as in a lightning study (Zheng et al., 2015), such burst series were acquired near perigee. In the last 10 days of the VAP mission, with perigees in the lower ionosphere, such burst series were acquired for almost every perigee passage.

3.2 Scalograms of VAP data bursts

The Matlab® continuous wavelet transform (CWT) function applied to burst mode L2 waveform data directly produces complex amplitudes over a logarithmically distributed range of frequencies. Scalogram plots in this work display the absolute value of the CWT amplitudes as a function of frequency at 28.6μs intervals such as in **figure 5**. The L2 waveform data is calibrated in amplitude at 1kHz only and has no phase calibration applied. Since calibration factors (University of Iowa, 2022) are only available for frequencies up to 11962.89 Hz, scalogram analysis is performed using L2 waveform data without phase calibration to examine frequency components all the way to the Nyquist frequency 17.5 kHz. The quality of the agreement between the dispersion curve and the nearly dispersionless whistler near 9:16 prior to the interpolated patch in this figure demonstrates that the lack of phase calibration at the highest frequencies is unimportant.

The 0.0315s dead time gap between successive bursts is filled in using linear interpolation between the last sample of a given burst and the first sample of an immediately succeeding burst. The representative scalogram shown in **figure 5** involves a pair of bursts concatenated with such linear interpolation. The primary artifact produced by this linear interpolation and concatenation is a suppression of high frequency components near the time of the interpolated patch of data, as best seen near the center time of the electric field scalograms in **figure 5**. In addition, the linear interpolation can enhance low frequency components, as best seen in **5f** near the center time, where there happens to be less confusion with other low frequency structures.

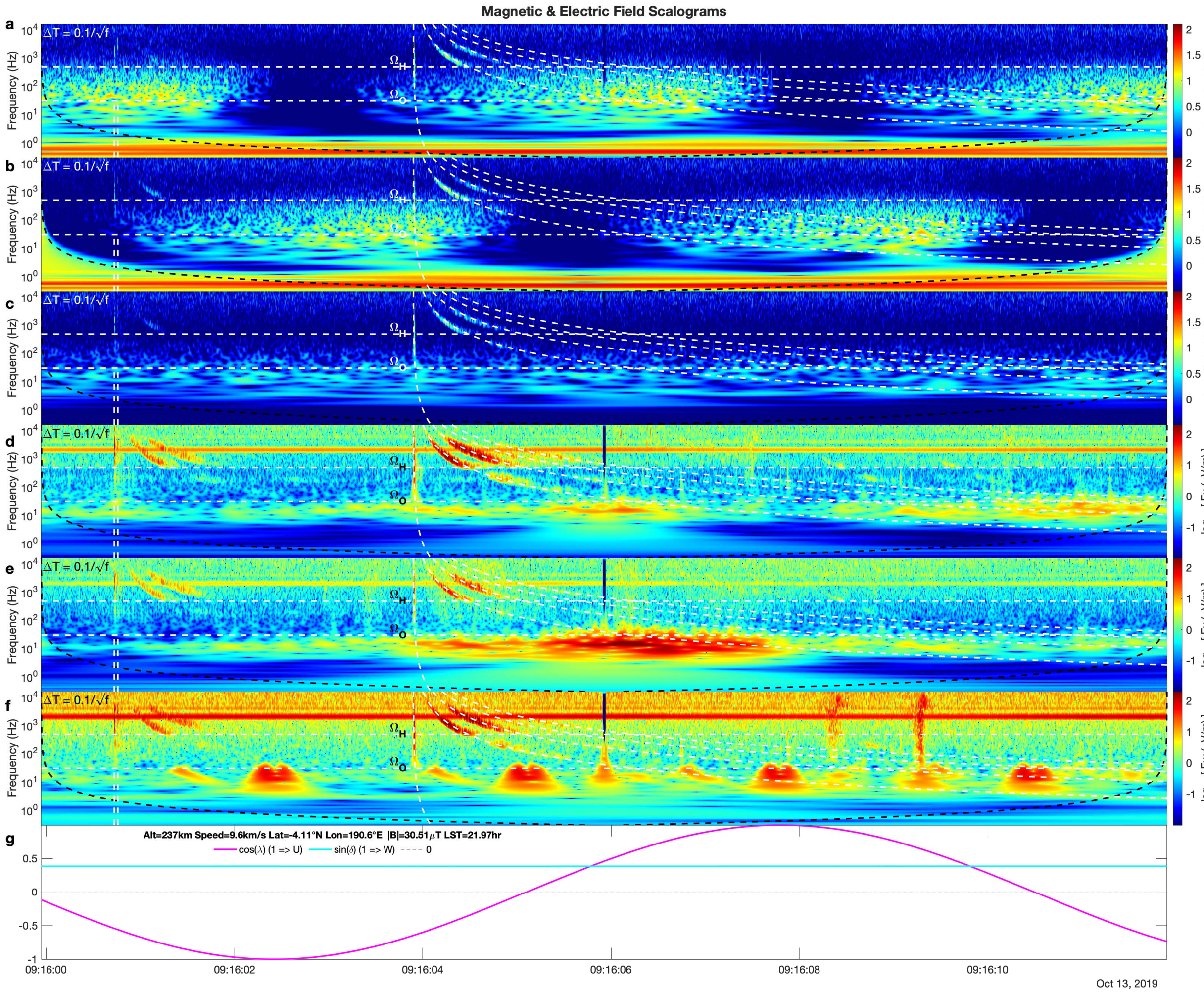

Figure 5. Scalograms for a representative consecutive pair of bursts are shown. In **a**, **b** and **c** scalograms for the U, V, and W components of magnetic field data are shown. In **d**, **e** and **f** the electric field scalograms are shown. In **g** the orientation of the probe spin vector is shown by the cyan and magenta curves. Horizontal white dashed lines are drawn for the cyclotron frequencies Ω_H and Ω_O. The curved dashed white lines drawn over the scalograms have $\Delta T = DC/\sqrt{f}$ with various dispersion constants (*DC*). The minimum *DC* value is shown in the upper left-hand corner of each scalogram. The two early sferics seen near 9:16:01 are marked with white vertical dashed lines extending only up to Ω_O in order not to obscure their signals at higher frequency. At frequencies below the cone of influence (COI) indicated by the curved black dashed lines superimposed on each scalogram plot, the amplitudes are derived under the assumption that the time variations in the burst data are symmetric about the boundaries at the start and end of the burst data. Below the COI, scalogram amplitudes must be viewed with caution. The nearly vanishing amplitudes seen in all components at the middle of the scalogram plots is an artifact of the linear interpolation across the dead time gap between successive bursts.

3.3 Spectrograms of Contiguous Bursts of VAP data

Fully calibrated spectra for successive series of 16384 data point samples are calibrated using the method and coefficients described in (University of Iowa, 2022). Each individual set of 16384 points produces a spectrum representing a 0.468s time interval. As the number of samples in a burst divided by 16384 = 12.75, approximately every 13th spectrum in a series of consecutive bursts is affected by the linear interpolation over the 0.0315s interval between bursts. The PSDs from contiguous data bursts are then integrated over the same series of logarithmically spaced bins as the onboard survey spectra to yield time and frequency dependent spectrograms of the mean square field values. Spectrogram plots display the mean square field values as a function of frequency at 0.468s intervals. A representative spectrogram from a set of 100 consecutive burst acquisitions near a typical perigee pass is shown in **figure 6**. Interpolation artifacts corresponding to those described in connection with **figure 5** are most readily apparent in the spectrograms during "quiet" and unstructured intervals, such as in the first few seconds of the E_u and E_v spectrograms in **6d** and **6e**, where a regular "picket fence" structure appears at low frequency corresponding to the artificial enhancement of low frequency power.

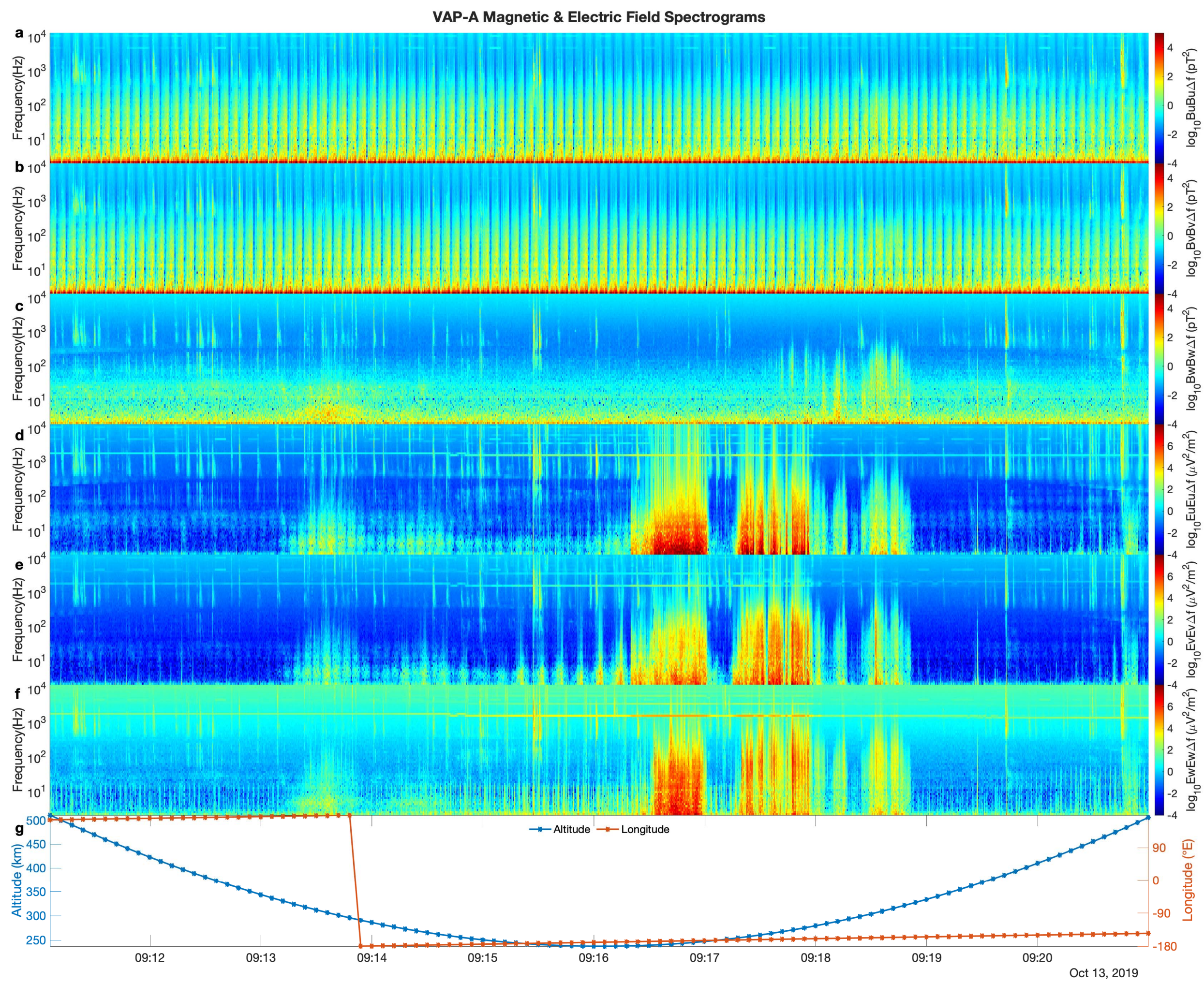

Figure 6. Spectrograms of the electromagnetic field from EMFISIS data are shown for a representative sample of Van Allen Probe-A (VAP-A) data. In **a**, **b**, and **c**, spectrograms for the three components (U, V and W) of the magnetic field are displayed. In **d**, **e** and **f**, electric field spectrograms are displayed. In **g** the altitude and longitude of VAP-A for each burst are plotted as a function of time.

3.4 Periodic Artifacts in Electric Field Data and a Mitigation Approach

A known (Kletzing et al., 2013) periodic artifact occurs when the axial boom on the side of the spacecraft pointing away from the Sun is periodically shadowed twice per spin period by the two magnetometer booms. This shadowing produces a pulse of approximately 0.3 s in the E_w component due to the sudden change in photoelectron current from the probe. In addition to this artifact, other disturbances appear at integer multiples of the spin period that primarily affect the E_w measurements. One of these artifacts manifests as brief intervals of increased scalogram intensity near $\cos(\lambda) = \pm 1$ and 0 in figure **5f** between 3 and 30Hz that recurs 4 times per spin period. Another artifact appears in figure **5f** is a pair of spikes extending up to the maximum frequency located at 9:16:08.4 and 9:16:09.3 that appear once per spin period for several cycles before and after the time shown in this figure. These artifacts wax and wane over series of bursts and produce features in E_w spectra that are not true plasma wave activity. However, because of the regularity of the periodic artifacts from burst to burst over successive cycles, their temporal extent within a given burst can be estimated and avoided. Artifacts produced by interpolation can also be avoided by avoiding the dead time between bursts. Several examples of fully calibrated spectra extracted from time intervals free of such artifacts are shown in **figure 7**.

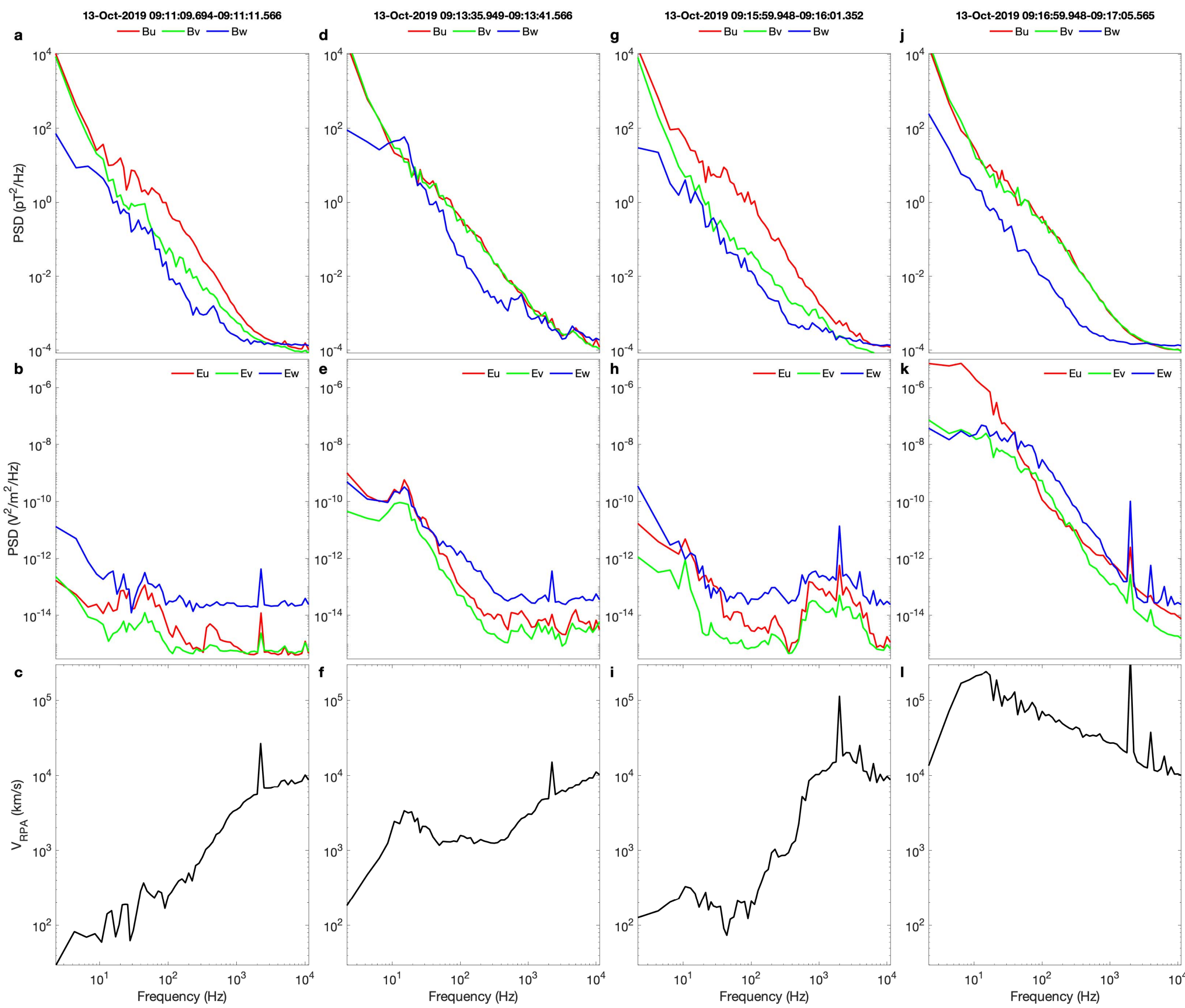

Figure 7. Representative fully calibrated spectra are displayed for four samples of data from the perigee pass spectrograms shown in the previous figure. Magnetic field spectra are shown in **a**, **d**, **g** and **j** with the time interval involved in each spectrum listed in the legend title for each case. Electric field spectra from the same four periods are shown in **b**, **e**, **h** and **k**. The RPA estimated upper limit on phase velocity as a function of frequency is shown in **c**, **f**, **i** and **l**.

3.5 Identification and Classification of Events and Waves

As can be seen in the previous three figures, the electric and magnetic fields exhibit several distinctive forms of activity. These include examples of all three modes ***F***, ***A*** and ***S*** of magnetohydrodynamic waves. In the next two sub-sections, the ***F*** and ***S*** cases are discussed. The ***A*** mode case is represented by the spectra shown in **figure 7d** and **e**, but further discussion is beyond the scope of this article.

3.5.1 Observation of *F* Waves, Echoes and Plasma Bubbles in Scalograms

By virtue of the high temporal resolution of the scalograms, WWLLN (Jacobson A. H., 2011) observed lightning strikes may be unambiguously identified with whistlers in VAP data. The WWLLN finds the time and location of individual lightning strikes with ~10km spatial accuracy, ~10µs temporal accuracy and ~90% efficiency for high peak current strikes (Holzworth, 2019). In **figure 5** three well isolated lightning strikes with strong low dispersion whistlers are seen. With the scalogram temporal resolution (28.6µs at the highest frequencies) the accidental correlation of low dispersion whistlers with the incorrect lightning strike (having a mean rate of ~ 60/s) is highly unlikely.

As evidenced by their adherence to dispersion curves of the form $\Delta T = DC/\sqrt{f}$ in **5a-f** for the strike at 9:16:03.893 located at an angular distance of 23.5° from the sub-satellite point, ***F*** mode waves are clearly being seen. The whistlers produced by this strike have dramatically differing dispersion functions. Each dispersion curves has been delayed by the 0.01s propagation delay through the EIWG from the strike location to the sub-satellite point. The four more highly dispersed whistlers are identified as subprotonospheric whistlers (Chum, 2009) which are echoes of reflections within the ionosphere as discussed earlier regarding the trapping region illustrated in **figure 4**. The curves shown have DC = 0.1, 12.6, 12.6*2, 12.6*3 and 12.6*4 $\text{Hz}^{1/2}$ s, consistent with dispersion constants for the echoes being proportional to the number of reflections.

The least dispersed whistler, despite having a *local* phase velocity (estimated from the ratio of the electric to magnetic field strengths) comparable to the other four whistlers, has a non-zero dispersion constant over two orders of magnitude less than the other whistlers. With less temporal resolution than available with EMFISIS, this whistler would be observationally dispersionless. This extremely low dispersion whistler implies that *for most of the path* between the source and VAP-A, its phase velocity was orders of magnitude faster than the other whistlers. This suggests the presence of a plasma bubble extending over most of the path, such as schematically illustrated in **figure 3**, within which the phase velocity could be 100 Mm/s or more, as is typical of the conditions near the EIWGUB shown in **figure 4**.

Further evidence that the more highly dispersed whistlers are echoes of waves that have travelled to higher altitude and back are the "gaps" in whistler intensity starting just below Ω_H and extending almost halfway to Ω_{He} which is midway between Ω_H and Ω_O on the logarithmic scale. These gaps are best seen for the DC = 12.6 and 12.6*2 $\text{Hz}^{1/2}$ s whistlers in **5d** and **f**. As first pointed out by (Gurnett et al., 1965), but using De Jonghe and Keppens (2021b) nomenclature, these gaps correspond to regions where ***F*** waves have been converted to ***A*** waves by passage through plasma having a significant concentration of H^+ ions. As shown in **figure 4a**, the concentration of H^+ ions are expected to be negligible at and below the VAP altitude during the acquisition of the data shown in **figure 5**, thus indicating that the wave echoes have travelled to higher altitude with higher H^+ concentrations prior to detection. The absence of ascending frequency ***A*** wave whistlers that would normally be seen in the gaps (Gurnett et al., 1965) in **figure 5** could be attributed to their attenuation along the echoing path.

The several orders of magnitude enhancements in the electric field spectra shown in **figure 7k** and the phase velocity in **7l** being so near the speed of light suggests that at this time, the satellite was immersed in a plasma bubble that extended all the way to the EIWG. Here the measured electric fields are typical of EIWG field strengths.

3.5.2 Observation of ***S*** waves in Magnetic Field Scalograms

In contrast to the electric field scalograms, the magnetic field fluctuations are generally much less dynamic and much more systematic in the ionosphere. The scalograms in **figure 5** show that the B_u and B_v fluctuations have components with clear periodic behavior that are 90° out of phase with each other. The VAP spin period during this data is 10.76 s, and is identical with the B_u and B_v fluctuation period seen directly in their variations in **5a** and **b**. The clear periodicity and 90° phase difference in the B_u and B_v fluctuations can also be seen in **figure 6a** and **b**, as well as their “insensitivity” to the substantial variations in the electric field variations.

These fluctuations at the VAP spin period in the magnetic scalograms of **figure 5a** & **b** are identified as ***S*** waves based on their speed. The upper limit on the speed of these waves derived from periods not having significant ***F*** wave activity such as in **figure 7c** and **7i** is so much less than $V_f = 609$ km/s for a primarily O^+ plasma (cf. **figure 1f**) that they can only be from ***S*** waves. Although *emitted* frequencies for V_s waves in an O^+ plasma do not extend above Ω_O, the large *DFR* factors of **expression 6** for $V_o/V_g = 9.6/1.4$ “kick” the *observed* frequencies far above Ω_O and could plausibly produce the $1/f^2$ spectral variation generally seen in the B_u and B_v spectra in **figure 7a**, **d**, **g** and **j** extending to a white noise floor at high frequency. The ***S*** mode assignment for these waves is further confirmed by their angular distribution. The absence of B_u activity near cos(λ)=±1 in **5a**, when the U axis is aligned with $\hat{\boldsymbol{B}}_\mathbf{0}$, and the absence of B_v activity near cos(λ)=0 in **5b** when the V axis is aligned with $\hat{\boldsymbol{B}}_\mathbf{0}$, is clear in these plots. As seen in **2c**, low frequency ***S*** wavevectors become insignificant in directions perpendicular to $\hat{\boldsymbol{B}}_\mathbf{0}$, so that ***S*** wave magnetic field fluctuations (that must be perpendicular to $\hat{\boldsymbol{k}}$) become insignificant in directions parallel to $\hat{\boldsymbol{B}}_\mathbf{0}$. The EMFISIS magnetic field fluctuation noise floor can be assessed from the intervals near the absence of ***S*** wave activity in the B_u data near cos(λ)=±1 in **5a** or in the B_v data near cos(λ)=0 in **5b**. In these intervals, the EMFISIS B field noise floor is found to be below 0.1 pT for frequencies between 3 and Ω_H.

The large doppler shift effects on the ***S*** wave activity precludes the possibility of observing possible resonance peaks in the VAP magnetic field spectra. However, the dependence of the doppler shifts on the orbital inclination suggests that magnetic field data from satellites in low earth *polar* orbits might be better suited for analysis of the spectral content of ***S*** wave activity. High-rate Swarm magnetic field data is particularly useful in this regard as discussed in section 4 below.

3.6 Systematics of ***S*** Wave Variations

The characteristic ***S*** wave activity seen in **figure 5a** & **b** is seen throughout the VAP mission and throughout the ionosphere. **Figure s1** in the supplemental materials showing the electric and magnetic field survey mode PSDs averaged over altitudes less than 1 Mm makes this clear. The intensity of this activity has clear correlation with geodetic location, as shown in **figure 8**. In this figure, the rms magnetic field fluctuations were computed from the calibrated spectra for every set of consecutive 16,384 samples available from perigee crossings during the last 10 days of the VAP mission. Altogether a total of 26,892 such rms values were available. The average rms values within 10km wide altitude bins, 30° wide longitude bins, and 1° wide latitude bins were computed for the plots shown. The peak seen in **figure 8** near 90°E, 5°S corresponds to a local maximum (Cecil et al., 2014) in the lightning rate, as expected for LG ***S*** waves. The systematic decrease of the intensity with altitude is consistent with these waves being generated below the satellite and experiencing some degree of attenuation as they propagate upwards.

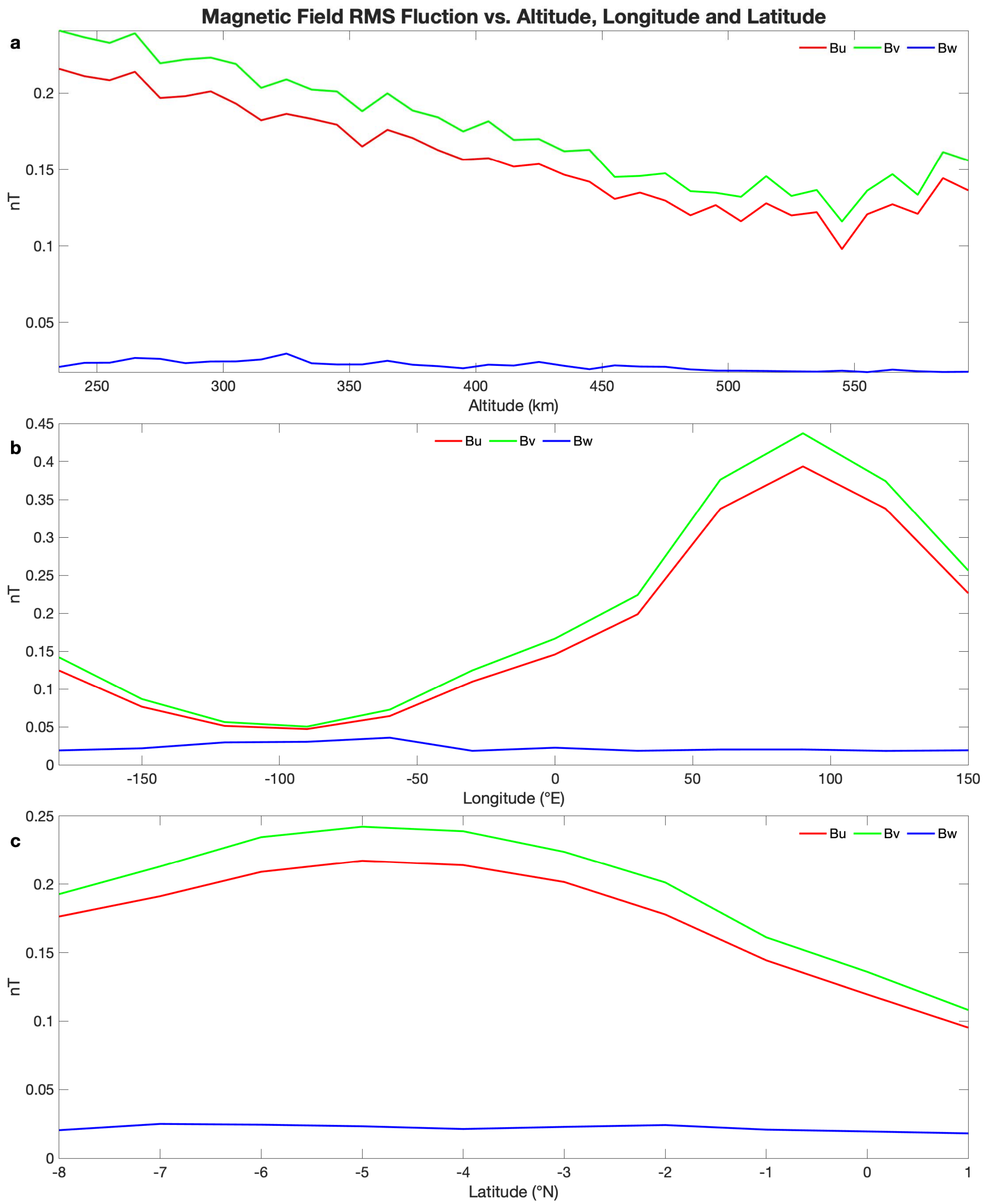

Figure 8. The correlation in rms magnetic field fluctuations with location is shown. The correlation with altitude is shown in **a**; with longitude in **b**; and with latitude in **c**.

4 Swarm Satellite Observations of Plasma Waves in the Ionosphere

The Swarm constellation of three nominally identical satellites: Alpha, Bravo and Charlie, (SwA, SwB and SwC) packed into a single bus were launched into a near polar orbit on 22 November 2013. By mid-March 2014, SwB was raised to its design altitude of approximately 525 km. The core instrument of the Swarm mission (Olsen et al., 2013) is the Vector Field Magnetometer (VFM). The VFM is a triaxial fluxgate magnetometer (Primdahl & Jensen, 1981) and (Merayo, 2014), consisting of three concentric spherical coils having mutually perpendicular axes. Three orthogonal sensor core coils within the spherical coils are provided to measure the three components of the magnetic field in directions determined by the coil orientation and highly insensitive to possible misalignments of the sensor coils. The sample rate of the VFM data is 50 Hz, thus a Nyquist frequency of 25 Hz. This frequency range of magnetic field fluctuations is especially well suited for the detection of ***S*** wave activity. The computation of scalograms and spectrograms from this data are performed as described above for the Van Allen Probe data.

For the first couple of months of the Swarm mission, SwA, B & C had a “beads on a string” orbital geometry, following each other very closely in space & time. During this phase, the spacing between the satellites gradually increased. Over the course of the next few months, SwA was lowered to its working altitude, SwB was raised to its working altitude and SwC was lowered to its working altitude. The orbital changes during this initial phase of the Swarm mission are indicated in **figure s2**.

At 21:01:30 on 14 March, 2014 two days after SwB was raised to its operational altitude of 525 km, a mysterious chirping in the high rate SwB VFM-y channel data as seen in **figure 9b** suddenly appeared. Exactly at the time that this chirping appeared, the overall noise level also suddenly increased *in the y channel*, as can be seen in the spectrograms. Near the time of this change in the y channel data, there was no similar change in either the x or z VFM channels. A systematic diurnal variation in the noise level in the x channel was seen, with greater noise in the afternoon and less noise in the pre-dawn. The overall increased SwB y channel noise level was not significantly different between the dayside and nightside of the orbits and did not depend on longitude. The mysterious chirping is found to be correlated with the alignment of the SwB velocity vector to the ambient magnetic field direction, as can be seen by comparison of figure sections **b** and **d** in this and in each of the similar figures shown in the supplemental materials.

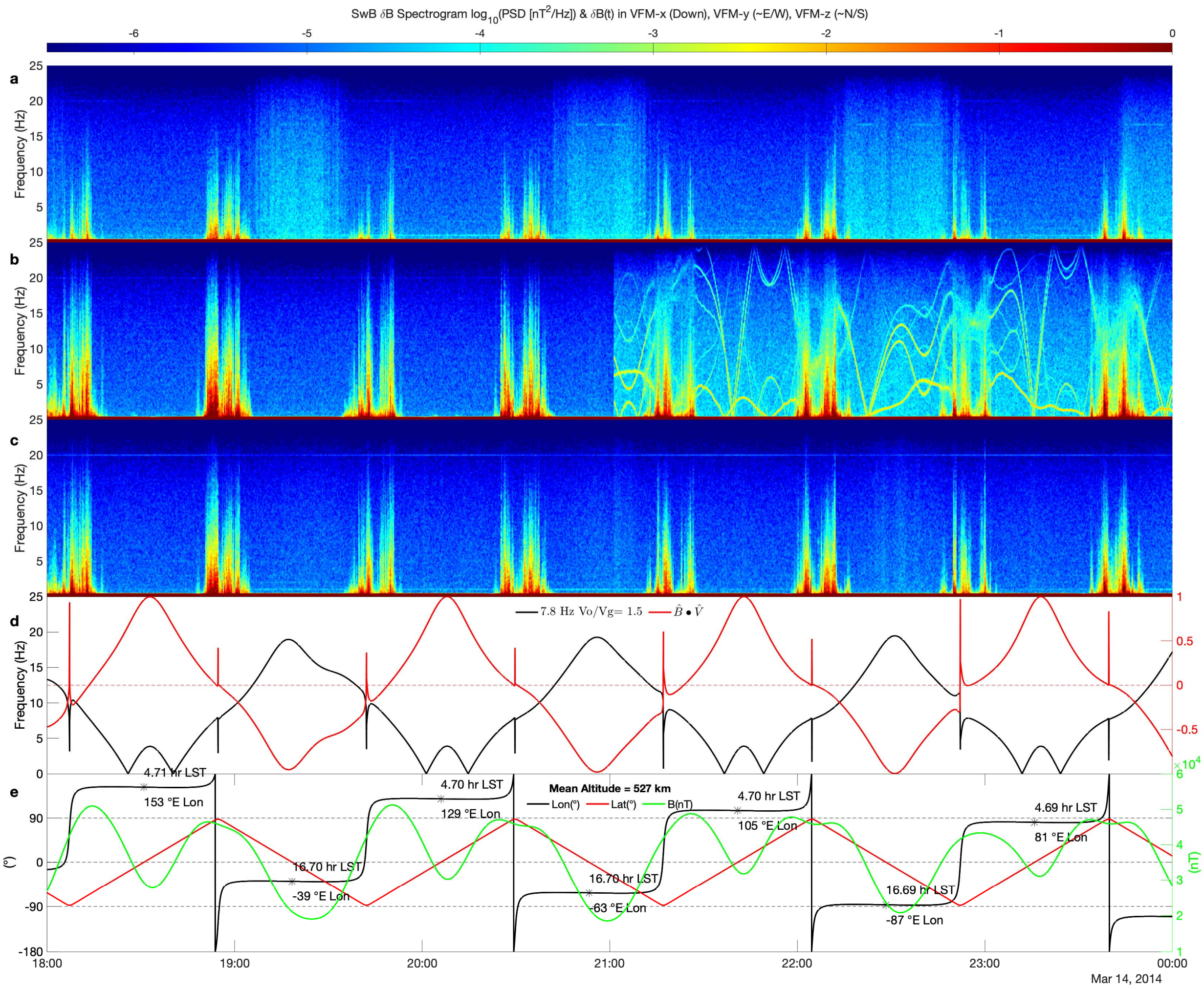

Figure 9. Spectrograms of data from the VFM magnetometers of the SwB satellite are shown for a six-hour period around the onset of chirping. In **a**, **b** and **c**, the VFM-x, -y and -z channel spectrograms are shown. In **d** the cosine of the angle between the local magnetic field and the satellite velocity vector is plotted in red with the ordinate scale on the right-hand side. Also plotted in black with ordinate on the left-hand side is a model of the doppler shifted fundamental Schumann resonance frequency. In **e** the latitude and longitude of SwB and the magnitude of the local magnetic field is plotted as a function of time. At each ascending or descending node (marked with asterisks) the local solar time and longitude are called out.

This chirping just as suddenly ceased at 11:17:53 on 25 June, 2014 as shown in **figure s3**. The cessation of chirping coincided with a manual power cycling of the VFM instrument on SwB. According to (European Space Research and Technology Centre, 2018), at the time that the chirping disappeared from the data, it is stated “70pT noise in y-measurement since [14 March 2014]”. After this power cycling, the overall background noise level in the y channel returned to that seen before the onset of chirping shown in **figure 9**. The overall background noise levels in the x and z channels did not significantly change after the power cycle.

Between 5:50 on 8 May 2014 and 7:20 on 9 May 2014, a series of four 90° yaw slew maneuvers of the SwB satellite were conducted and after each of the 90° yaw slews the observed chirping ***apparently*** transforms back and forth between the East-West and North-South directions. Throughout the entire time the chirping is observed, however, it is confined to the single VFM-y channel. Data from the interval around the first yaw slew is shown in **figure s4**. During the slew process the various resonant frequencies are disturbed. After the slew completes, the character of the resonance variations matches the character before the slew began. Very similar variations happen for the subsequent three slew maneuvers.

It is suggested here that the unusual SwB VFM-y signals are not instrumental artifacts, but rather signals produced by doppler shifted resonances. In support of this, the centroid of the distribution of doppler shifted frequencies using **expression 7** for the lowest Schumann resonance frequency of 7.8 Hz is plotted with the assumption of a *fixed* value for the ratio of V_o/V_g. With the SwB speed being 7.6 km/s, and with a speed for H^+ plasma waves at the 525km SwB altitude of approximately 5 km/s, as shown in **figure 4** for example, V_o/V_g is approximately 1.5, but without detailed measurements of the ionospheric composition and temperature, this is only an estimate. Even so, the strongest of the resonance features seen in **figure 9** qualitatively follows the behavior of the doppler shifted frequency variation. Note, for example, that the observed frequency of this resonance in **9b** appears to pass through zero, reaching a minimum negative value near 21:40, but because the measured frequencies are restricted to positive values between 0 and 25 Hz, the would be negative "valley" appears as a positive peak. Also, at times that the spacecraft passes over the magnetic poles, where the local magnetic field is vertical, such as at the times 22:05, 22:52 and 23:40, according to **expression 7**, the centroid of the doppler shift distribution is unshifted and the width of the distribution becomes maximal.

Surrounding the crossing of the magnetic poles, upon passage through the auroral regions as described by (McGranaghan et al., 2017), field aligned currents (FACs) produce significant fluctuations in the magnetic fields. These disturbances are seen in all VFM components, but there is a region inside the auroral oval where the FAC disturbance is not so dominant, and the appearance of the unshifted, but broadened fundamental Schumann resonance frequency becomes apparent. Among the polar crossings in **figure 9**, the case at 22:05 shows the clearest evidence for the lowest SR frequency with the case at 23:40 displaying similar behavior. In the supplemental **figure s3**, at 8:06 a particularly clean auroral oval center region shows the lowest SR frequency following the simple doppler shift model. It can generally be seen that the resonances indeed appear broader near the poles than near the equator, as predicted by **expression 7**.

There are several resonance features in the SwB VFM-y channel data beyond the SR fundamental. Without more accurate knowledge of the ionospheric composition, its temperature and possible bulk plasma drift velocities, it is not feasible to precisely model these features, such as the higher SR resonances or other possible ionospheric resonances. Finally, a more subtle feature of the chirping in the data is that each of the resonance features appears to have a fainter "echo" at exactly 25 Hz minus the frequency of the resonance. This is clearest in **9b** near 21:00, for example, but this echo is present throughout **figures 9**, **s3**, and **s4**. It is suspected that these echoes are indeed instrumental artifacts.

Less direct evidence in support of the reality of the existence of the resonances in the SwB data is that the rms magnetic field fluctuations seen in the SwB VFM-y channel data during the time that the mysterious resonances are seen is typically between 0.1 and 0.2 nT. This value is consistent with the magnetic field fluctuations measured at the SwB altitude with the VAP, as shown in **figure 8**. On the other hand, for the other VFM channels, and for the other Swarm satellites, the magnetic field noise level is much less, and is NOT consistent with the expectations from the far more sensitive EMFISIS data. It appears that for most of the Swarm mission, there was apparently an effective low pass filter involved in the data processing that precludes the ability to measure the resonances described here.

5 Conclusions

Evidence for a persistent population of slow magnetosonic waves in the ionosphere has been presented. Evidence for the presence of a small number of resonances in these waves has also been found. The intensity of the electric field disturbances seen in the Van Allen probe data near suggested plasma bubbles are consistent with the intensities of (Ni & Zhao, 2005). The intensity of the magnetic field resonances seen in Swarm Bravo data is also consistent with their results. The strong dependence on doppler shift effects on the inclination of satellite orbits can explain differences between Van Allen probe and Swarm observations of low-speed magnetic field plasma waves. Although the point that the magnetic field resonances seen here in the Swarm data and by Ni & Zhao cannot be simple leakage of magnetic Schumann Resonances from the Earth ionosphere waveguide (EIWG) is well taken since they are so strong, this does not prove that these waves could not have been produced by the conversion of electric field oscillations to slow magnetosonic waves in the complex interaction region of the EIWG upper boundary.

If the suggestions of this work are accepted, some of the discrepancy between model and along-track magnetic field difference observations tabulated by (Finlay et al., 2020) could perhaps be produced by these waves. Better knowledge of these hitherto unremarked plasma structures in the ionosphere could perhaps help better understand and interpret past and future satellite measurements of the earth's magnetic field and ionospheric plasma wave activity.

Acknowledgments, Samples, and Data

Van Allen Probes wave data used in this paper can be found in the EMFISIS archive (http://emfisis.physics.uiowa.edu/data/index) and the work of the EMFISIS team in its production is gratefully acknowledged. Swarm data used in this paper is provided by the European Space Agency and can be accessed online at https://swarm-diss.eo.esa.int. The author thanks Jordi De Jonghe for helpful discussion, especially regarding dispersionless wave propagation analysis.

References

Works Cited

Alken, P. e. (2021). International Geomagnetic Reference Field: the thirteenth generation. *Earth, Planets and Space*, doi:10.1186/s40623-020-01288-x.

Beggan, C. B. (2017, March). *Magnetic Schumann Resonances in Swarm ASM Burst Mode, VFM HF and e-POP Data?* Retrieved from British Geological Survey, Natural Environment Research Council: http://nora.nerc.ac.uk/id/eprint/517050/1/Beggan_Banff2017%20(002).pdf

Boldi, R. W. (2017). Determination of the Global-Averal Charge Moment of a Lightning Flash Using Schumann Resonances and the LIS/OTD Lightning Data. *JGR: Atmospheres*, doi:10.1002/2017JD027050.

Budden, K. (1957). The "wave-guide" Mode Theory of the Propagation of Very-Low-Frequency Radio Waves. *Proceedings of the IRE*, doi:10.1109/JRPROC.1957.27847.

Burgesser, R. (2017). Assessment of the World Wide Lightning Location Network (WWLLN) detection efficiency by comparison to the Lightning Imaging Sensor (LIS). *Quarterly Journal of the Royal Meteorological Society*, doi:10.1002/qj.3129.

Cecil, D. B. (2014). Gridded lightning climatology from TRMM-LIS and OTD: Dataset description. *Atmospheric Research*, doi:10.1016/j.atmosres.2012.06.028.

Chapman, F. L. (1966). Observation on the propagation constant of the Earth-ionosphere waveguide in the frequency band 8 c/s to 16 kc/s. *Radio Science*, doi:10.1002/rds19661111273.

Chen, L. a. (2012). Perpendicular propagation of magnetosonic waves. *Geophysical Research Letters*, doi:10.1029/2012GL052485.

Chum, J. S. (2009). Analysis of subprotonospheric whistlers observed by DEMETER-A case study. *Journal of Geophysical Research*, doi:10.1029/2008JA013585.

COSPAR. (2022, 1). Retrieved from International Reference Ionosphere: http://irimodel.org

European Space Research and Technology Centre. (2018, 3 31). *Swarm Spacecraft Anomalies and Manoeuvres History (till 31 March 2018).* Retrieved from https://earth.esa.int/eogateway/documents/20142/37627/Swarm_manoeuvres.pdf/5e7ccf65-67ec-2d1a-6e65-d6d4bd7ee032

Finlay, C. K.-C. (2020). The CHAOS-7 geomagnetic field model and observed changes in the South Atlantic Anomaly. *Earth, Planets and Space*, doi:10.1186/s40623-020-01252-9.

Friis-Christensen, E. L. (2006). Swarm: a constellation to study the Earth's magnetic field. *Earth Planets Space*, doi:10.1186/BF03351933.

Fullekrug, M. (1995). Schumann resonances in magnetic field components. *Journal of Atmospheric and Terrestrial Physics*, doi:10.1016/0021-9169(94)00075-Y.

Fullekrug, M. a.-S. (1996). Further evidence for a global correlation of the Earth-ionosphere cavity resonances. *Geophysical Research Letters*, doi:10.1029/96GL02612.

Goedbloed, H. K. (2019). *Magnetohydrodynamics of Laboratory and Astrophysical Plasmas.* Cambridge, United Kingdom: Cambridge University Press.

Gurnett, D. S. (1965, April 1). Ion Cyclotron Whistlers. *Journal of Geophysical Research, 70*(7), 1665-1688.

Holzworth, R. M. (2019). Global Distribution of Superbolts. *Journal of Geophysical Research: Atmospheres*, doi:10.1029/2019JD030975.

Jackson, J. (1975). *Classical Electrodynamics.* New York: John Wiley & Sons.

Jacobson, A. H. (2006). Performance Assessment of the World Wide Lightning Location Network (WWLLN), Using the Los Alamos Sferic Array (LASA) as Ground Truth. *Journal of Atmospheric and Oceanic Technology*, doi:10.1175/JTECH1902.1.

Jacobson, A. H. (2011). Study of oblique whistlers in the low-latitude ionosphere, jointly with the C/NOFS satellite and the World-Wide Lightning Location Network. *Ann. Geophys.*, doi:10.5194/angeo-29-851-2011.

Jonghe, J. a. (2020a). A two-fluid analysis of waves in a warm ion-electron plasma. *Plys. Plasmas*, doi:10.1063/5.0029534.

Jonghe, J. a. (2020b). Two-Fluid Treatment of Whistling Behavior and the Warm Appleton-Hartree Extension. *JGR Space Physics*, doi:10.1029/2020JA028953.

Kletzing, C. e. (2013). The Electric and Magnetic Field Instrument Suite and Integrated Science (EMFISIS) on RBSP. *Space Science Reviews*, doi:10.1007/s11214-013-9993-6.

Mauk, B. e. (2013). Science Objectives and Rationale for the Radiation Belt Storm Probes Mission. *Space Sci Rev*, doi:10.1007/s11214-012-9908-y.

McGranaghan, R. M. (2017). A Comprehensive Analysis of Multiscale Field-Aligned Currents: Characteristics, Controlling Parameters, and Relationships. *Journal of Geophysical Research: Space Physics*, doi:10.1002/2017JA024742.

Merayo, J. M. (2014, June 19-20). The Swarm Vector Field Magnetometer (VFM): instrument comissioning and performance assessment. *3rd Swarm Science Meeting* (pp. 1-18). Copenhagen, Denmark: DTU Space National Space Institute.

Ni, B. a. (2005). Spatial Observations of Schumann Resonace at the Ionospheric Altitudes. *Chinese Journal of Geophysics*, doi:10.1002/cjg2.719.

Nickolaenko, A. a. (2004). Time domain presentation for ELF pulses with accelerated convergence. *Geophysical Research Letters*, doi:10.1029/2003GL018700.

Nickolaenko, A. H. (2008). Q-bursts: A comparison of experimental and computed ELF waveforms. *Radio Science*, doi:10.1029/2008RS003838.

Ogawa, T. T.-S. (1967). Worldwide Simultaneity of Occurrence of a Q-type ELF Burst in the Schumann Resonance Frequency Range. *Journal of Geomagnetism and Geoelectricity*, doi:10.5636/jgg.19.377.

Olsen, N. e. (2013). The Swarm Satellite Constellation Application and Research Facility (SCARF) and Swarm data products. *Earth Planets Space*, doi:10.5047/eps.2013.07.001.

Price, C. (2016). ELF Electromagnetic Waves from Lightning: The Schumann Resonances. *Atmosphere*, doi:10.3390/atmos7090116.

Primdahl, F. a. (1981). Compact spherical coil for fluxgate magnetometer vector feedback. *J. Phys. E: Sci. Instrum.*, doi:10.1088/0022-3735/15/2/015.

Rodriguez-Camacho J., S. A.-C.-R. (2021). Four Year Study of the Schumann Resonance Regular Variations Using the Sierra Nevada Station Ground-Based Magnetometers. *Journal of Geophysical Research: Atmospheres*, doi:10.1029/2021JD036051.

Salinas, A. T.-R.-C. (2016). Solar storm effects during Saint Patrick's Days in 2013 and 2015 on the Schumann resonances measured by the ELF station at Sierra Nevada (Spain). *Journal of Geophysical Research: Space Physics*, doi:10.1002/2016JA023253.

Santolik, O. P. (2009). Propagation of unducted whistlers from their source lightning: A case study. *JGR*, doi:10.1029/2008JA013776.

Satori, G. (1996). Monitoring Schumann resonances-II. Daily and seasonal frequency variations. *Journal of Atmospheric and Terrestrial Physics*, doi:10.1016/0021-9169(95)00146-8.

Schumann, W. (1952). On the free oscillations of a conducting sphere which is surrounded by an air layer and an ionosphere shell (in German). *Z. Naturforsch. B, 7A*, 149-154.

Sentman, D. (1987). Magnetic elliptical polarization of Schumann resonances. *Radio Science*, doi:10.1029/RS022i004p00595.

Shapiro, N. a. (2004). Emergence of broadband Rayleigh waves from correlations of the ambient seismic noise. *Geophysical Research Letters*, doi:10.1029/2004GL019491.

Simoes, F. P. (2011). Satellite observations of Schumann resonances in the Earth's ionosphere. *GRL*, doi:10.1029/2011GL049668.

Surkov, V. N. (2013). Penetration of Schumann resonances into the upper atmosphered. *Journal of Atmospheric and Solar-Terrestrial Physics*, doi:10.1016/j.jastp.2013.02.015.

Toffner-Clausen, L. L. (2016). In-flight scalar calibration and characterisation of the Swarm magnetometry package. *Earth, Planets and Space*, doi:10.1186/s40623-016-0501-6.

University of Iowa. (2022). *Waveform Calibrations*. Retrieved from EMFISIS An instrument suite on the Van Allen Probes: https://emfisis.physics.uiowa.edu/Waveform_Calibration

Woodman, R. (2009). Spread F - an old equatorial aeronomy problem finally resolved? *Ann. Geophys.*, doi:10.5194/angeo-27-1915-2009.

Zheng, H. e. (2015). A statistical study of whistler waves observed by Van Allen Probes (RBSP) and lightning detected by WWLN. *Journal of Geophysical Research: Space Physics*, doi:10.1002/2015JA022010.

Journal of Geophysical Research: Space Physics

Supporting Information for

A Novel Population of Slow Magnetosonic Waves in the Ionosphere

Charles L. Bennett[1]

[1]Retired from Lawrence Livermore National Laboratory

Contents of this file

Text S1
Figures S1 to S4

Introduction

The text S1 in this supporting information provides a derivation of expression 7 in the main text.

The figures in this supporting information file supplement the main document.

Text S1.

Expression 6 from the main text is

$$DFR = \frac{\omega_o}{\omega} = 1 - \frac{V_o}{V_g}\frac{\hat{\boldsymbol{k}}\cdot\hat{\boldsymbol{V}}_o}{\hat{\boldsymbol{k}}\cdot\hat{\boldsymbol{B}}_0}\,. \quad (6)$$

This involves the ratio of the dot products of unit vectors $\hat{\boldsymbol{k}}\cdot\hat{\boldsymbol{V}}_o$ and $\hat{\boldsymbol{k}}\cdot\hat{\boldsymbol{B}}_0$. The velocity and magnetic field vectors determine a plane. In the following, let the x axis be along the magnetic field direction and let the velocity vector be at an angle γ with respect to the magnetic field direction. The unit velocity vector in the x-y plane has coordinates

$$[\cos(\gamma), \sin(\gamma)],$$

so that for a unit wavevector $\hat{\boldsymbol{k}}$ in the x-y plane given by $[\cos(\theta), \sin(\theta)]$, the ratio of the dot products in expression (6) is

$$[\cos(\gamma)\cos(\theta)+ \sin(\gamma)\sin(\theta)]/\cos(\theta) = \cos(\gamma)+ \sin(\gamma)\tan(\theta).$$

Since components of the wavevector in the z direction orthogonal to the x-y plane make no difference to the DFR, without loss of generality, it can be assumed that the wavevector is confined to the x-y plane. The expression for the DFR in (6) has a central value that is independent of the wavevector direction θ given by

$$DFR=1- \cos(\gamma)\ V_o/V_g\ .$$

The spread of the DFR values about this central value is determined by $t=\tan(\theta)$. Although angles θ near $\pm\pi/2$ produce very large DFR values, the resulting DFR values are widely spread per unit change in θ. For a uniformly distributed random set of wave vector directions, the density of DFR values is given by the derivative of the arctangent function

$$\frac{d}{dt}\arctan(t) = \frac{1}{(1+t^2)}\ .$$

After supplying the offsets and scaling factors, this leads to the probability distribution in expression 7 of the main text

$$pdf \propto \frac{1}{\left(DFR-1+\frac{V_o}{V_g}\cos(\gamma)\right)^2+\left(\frac{V_o}{V_g}\sin(\gamma)\right)^2}\ . \tag{7}$$

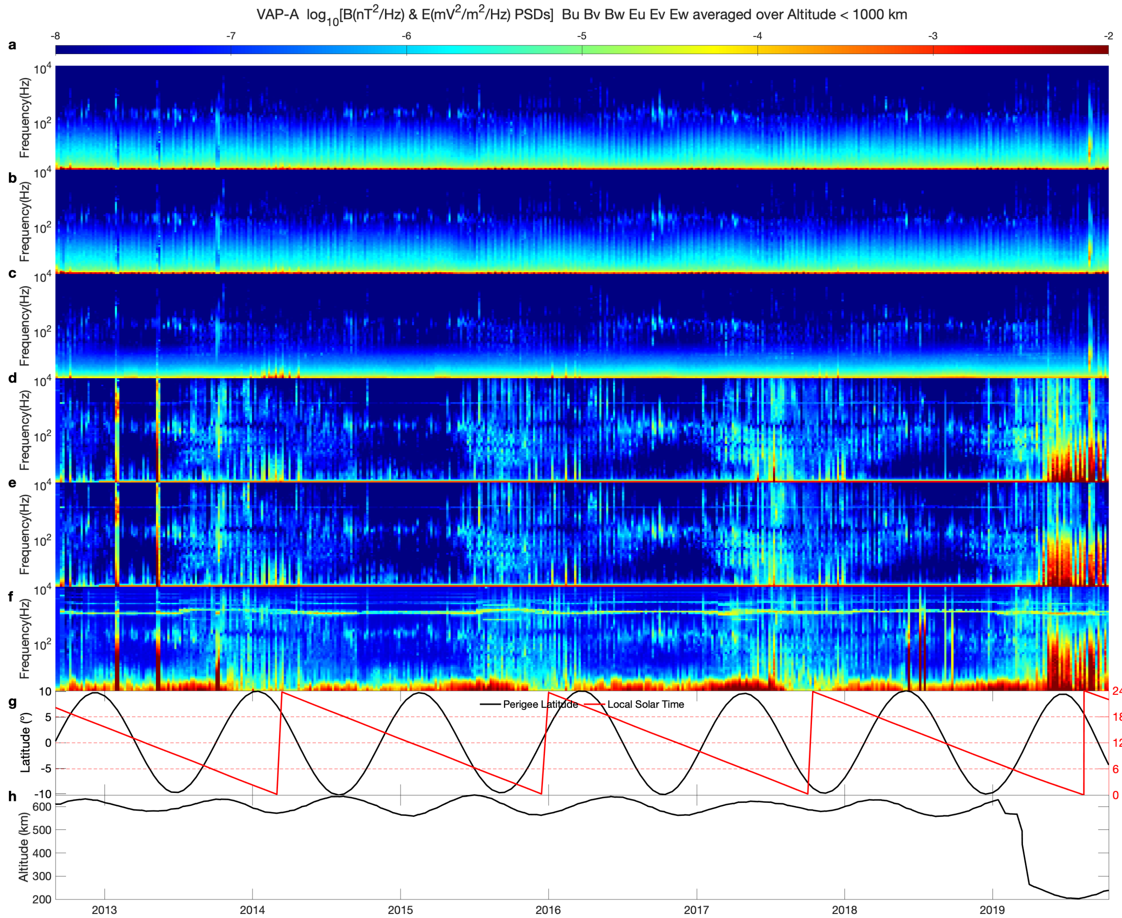

Figure S1. **The long term variations in electric and magnetic ionospheric PSDs derived from the survey data are shown. For the 1st and 14th of each month throughout the VAP mission, the mean PSD over altitudes less than 1 Mm is computed from the survey mode data and displayed as a function of frequency. In a, b and c the Bu, Bv and Bw PSDs are shown. In d, e and f the Eu, Ev and Ew PSDs are shown. In g the latitude and local solar time of perigee are shown. In h the altitude of perigee is shown.**

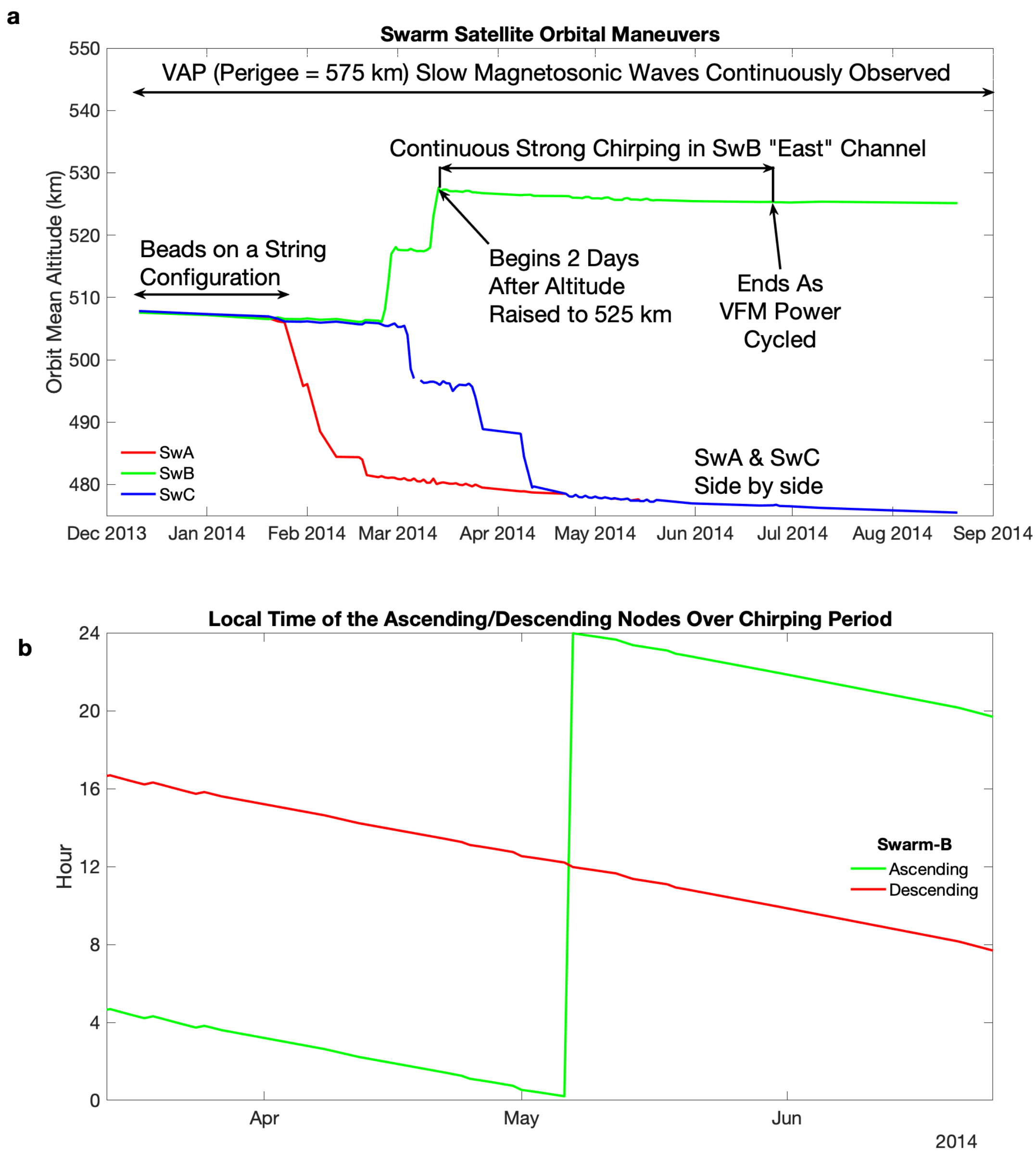

Figure S2. The initial development of the Swarm constellation configuration is illustrated. In a, the altitudes for SwA, B and C are shown as a function of time. In b, the local time of the ascending and descending nodes for the SwB satellite are shown.

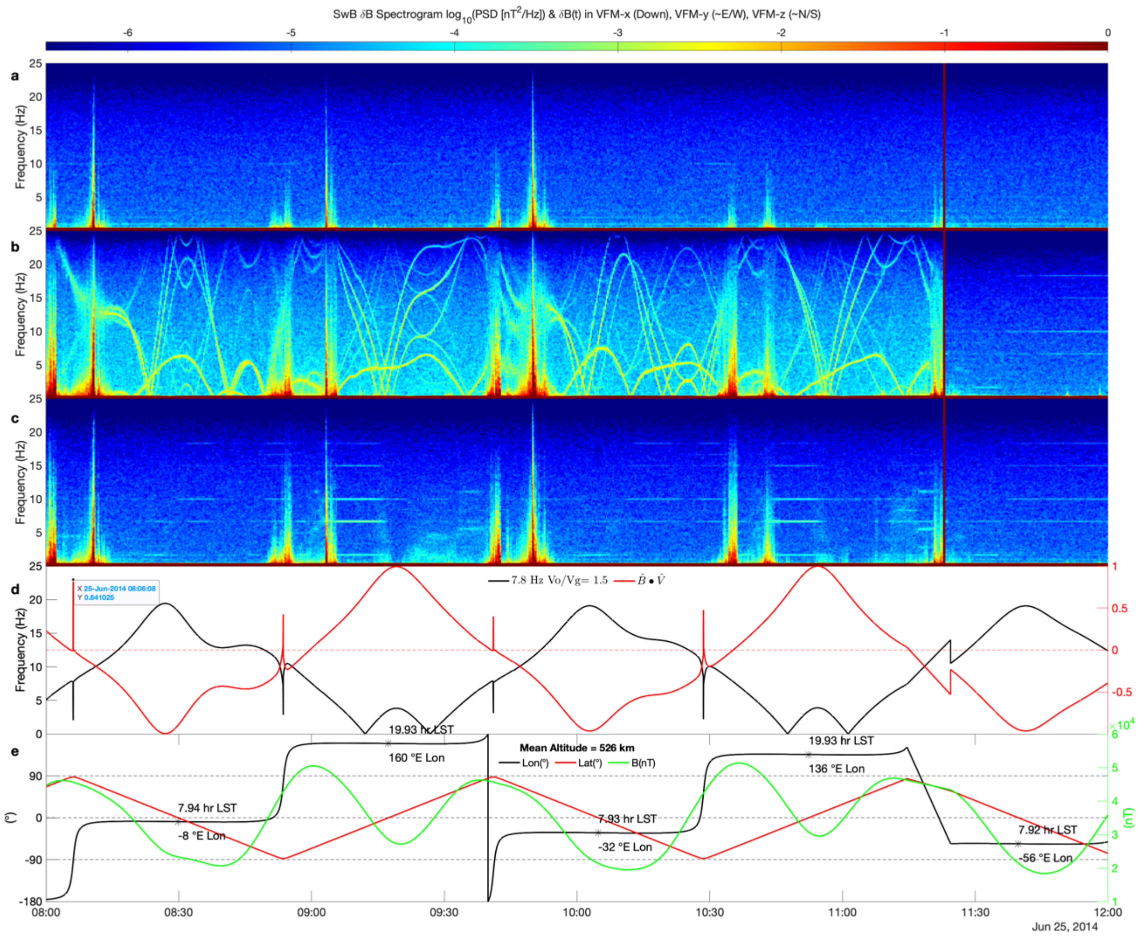

Figure S3. Spectrograms of data from the VFM magnetometers of the SwB satellite are shown near the time of the cessation of chirping. In a, b & c the VFM-x, y and z channels spectrograms are shown. In d the cosine of the angle between the local magnetic field and the satellite velocity vector is plotted in red with the ordinate scale on the right hand side. Also plotted in black with ordinate scale on the left hand side is a model of the doppler shifted fundamental Schumann resonance frequency. In e the latitude and longitude of SwB and the magnitude of the local magnetic field is plotted as a function of time. At each ascending or descending node (marked with asterisks) the local solar time and longitude are called out.

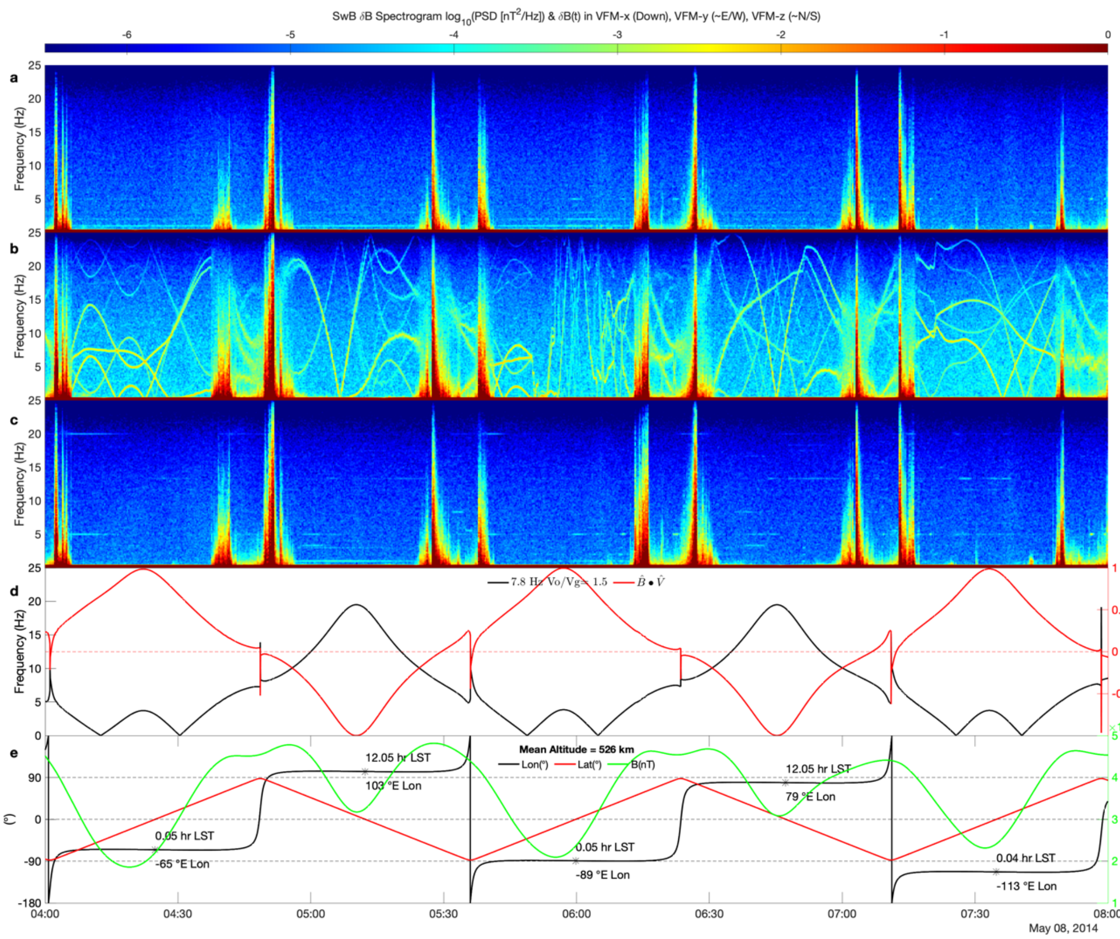

Figure S4. VFM spectrograms are shown near the first yaw slew maneuver. The layout is the same as the previous figure.